Spring 5-15-2017

Underwater Celestial Navigation Using the Polarization of Light Fields

Samuel Bear Powell
Washington University in St. Louis

Recommended Citation

Powell, Samuel Bear, "Underwater Celestial Navigation Using the Polarization of Light Fields" (2017). *Engineering and Applied Science Theses & Dissertations*. 245.
https://openscholarship.wustl.edu/eng_etds/245

WASHINGTON UNIVERSITY IN ST. LOUIS
School of Engineering & Applied Science
Department of Computer Science and Engineering

Dissertation Examination Committee:
Roger Chamberlain, Chair
Mark Anastasio
Shantanu Chakrabarrty
Ron Cytron
Roman Garnett
Viktor Gruev

Underwater Celestial Navigation Using the Polarization of Light Fields

by
Samuel Bear Powell

A dissertation presented to
The Graduate School
of Washington University in
partial fulfillment of the
requirements for the degree
of Doctor of Philosophy

May 2017
St. Louis, Missouri

Table of Contents

List of Figures

List of Tables

Acknowledgements

This work would not have been possible without the support of my friends, family, and colleagues. I would especially like to thank Professor Viktor Gruev, for getting me started on research as an undergraduate student and for advising me throughout my graduate studies, and Professor Ron Cytron, for introducing me to Viktor when I was looking for a summer job 7 years ago.

Funding for this work was provided by the National Science Foundtion, grant numbers OCE-1130897, 0905368, OCE-1636028, and 1603933, and by the U.S. Air Force Office of Scientific Research, grant numbers FA9550-10-1-0121 and FAA9550-12-1-0321.

Samuel Bear Powell

Washington University in St Louis

May 2017

Dedicated to you, dear reader.

ABSTRACT OF THE DISSERTATION

Underwater Celestial Navigation Using the Polarization of Light Fields

By

Samuel Bear Powell

Doctor of Philosophy in Computer Engineering

Washington University in St. Louis, 2017

Professor Roger Chamberlain, Chair

Global-scale underwater navigation presents challenges that modern technology has not solved. Current technologies drift and accumulate errors over time (inertial measurement), are accurate but short-distance (acoustic), or do not sufficiently penetrate the air-water interface (radio and GPS). To address these issues, I have developed a new mode of underwater navigation based on the passive observation of patterns in the polarization of in-water light. These patterns can be used to infer the sun's relative position, which enables the use of celestial navigation in the underwater environment. I have developed an underwater polarization video camera based on a bio-inspired polarization image sensor and the image processing and inference algorithms for estimating the sun's position. My system estimates heading with RMS error of 6.02° and global position with RMS error of 442 km. Averaging experimental results from a single site yielded a 0.38° heading error and a 61 km error in global position. The instrument can detect changes in polarization due to a 0.31° movement of the sun, which corresponds to 35.2 km of ground movement, with 99% confidence. This technique could be used by underwater vehicles for long-distance navigation and suggests additional ways that marine animals with polarization-sensitive vision could perform both local and long-distance navigation.

Chapter 1: Introduction

1.1 The Challenges of Underwater Navigation

Humans have been navigating over land and water for thousands of years, and in the air for almost 100 [1]. Over this time, we have developed a wide variety of navigation techniques, which can be broadly grouped in the three catagories: pilotage, celestial navigation, and intertial navigation [2]. However, most of our navigation techniques suffer severe limitations when operating in an underwater environment.

Pilotage is probably the most common form of navigation throughout history—it is the art of determining one's location from observations of known landmarks, from memory or by comparing them to a map or chart. Modern pilotage is assisted by both active beacons and active observation technologies: beacons include lighthouses, LORAN (now obsolete), and VOR (the system used for commercial air travel). Active observation technologies include RADAR, LIDAR, and SONAR. With technological assistance pilotage techniques are highly accurate and robust, but only provide regional navigation and require local knowledge. In the underwater environment, however, the theoretical maximum visibility is only 80 meters, which severely limits navigation by landmarks [3]. Radio techniques enjoy a larger range, but are still limited by the high propagation loss of sea water—practical radio communications can only reach ranges of 1 km underwater [4]. Additionally, the high reflectivity of the air-water interface prevents terrestrial radio beacons from penetrating to any practical depth [5, 6]. SONAR and acoustic beacons are the best choice in the underwater environment as their attenuation is orders of magnitude less than radio [7], but they are still limited to ranges on the order of several kilometers [8]. Bottom-lock Doppler SONAR can be used for long-range navigation, but requires the vehicle to remain within 100 meters of the sea-floor, limiting its practicality [9].

Celestial navigation is similar to pilotage, but rather than observe fixed landmarks, one measures the apparent positions of celestial objects such as the sun, moon, and stars. With sufficient knowledge of their movement relative to the Earth it is possible to determine where on the globe the measurements were taken. Traditionally, the measurements and computations for celestial navigation required great skill, making it practical only for long-distance ocean voyages. However, there are now artificial satellite systems, such as the US Navstar GPS constellation, for providing high precision global navigation to anyone with a receiver [10]. Again, however, these techniques are stymied by the low visibility and high electromagnetic losses of the underwater environment.

Finally, inertial navigation, or “dead reckoning,” is navigation based on integrating observations of one’s internal state over time to determine changes in position—i.e. counting your steps with your eyes closed. MEMS accelerometers and gyroscopes provide low-cost inertial sensing for dead-reckoning, while advanced ring-laser gyroscopes and laser accelerometers enable very high accuracy navigation for more critical applications [11, 12]. Inertial navigation systems (INSs) tend to provide higher frequency position information than pilotage or celestial navigation systems, but they suffer from unbounded errors. Any noise or drift in the sensor readings will be integrated along with the true inertial state, leading to navigation errors that increase over time even when not moving [13]. Thus, such systems are typically used in conjunction with pilotage or celestial navigation technologies: the integrated inertial errors can be zeroed periodically using readings from other systems, while the INS measurements can be used to keep track of position between updates [2]. Fortunately, INS systems are not directly limited by operating underwater, but underwater vehicles that use inertial sensors still need to regularly zero their errors. This often requires surfacing and acquiring a GPS lock before submerging again [14], which is a waste of time and energy, and potentially a tactical risk for covert underwater vehicles.

1.2 A Biological Strategy: Using Polarization for Navigation

When faced with a challenging engineering task, it is often worthwhile to investigate the strategies that animals have evolved for solving the same problem. Evolved systems tend to be both efficient and robust, as natural selection favors individuals who can complete tasks more quickly, using less energy, and under a wide variety of conditions. Many animals, including marine animals, regularly navigate long distances [15], by studying their behavior and environment we can gain insight into potential technical solutions.

Many terrestrial animals are known to use the polarization of the sky as a compass cue for navigation. It has been well-documented that certain arthropods—such as ants, bees, crickets, dung beetles, and spiders—have photoreceptor arrays specifically sensitive to the patterns of polarized light in the sky, which they use as a compass [16-19]. Honey bees, for example, can use the polarization from a single patch of sky on an otherwise cloudy day to navigate to and from their hive [17]. There is also evidence that some birds may use the polarization of the sky at dawn and dusk to calibrate their magnetic compasses during long-range migrations [20, 21].

The polarization patterns of underwater light have similar structure to the polarization patterns of the sky, and follow predictable trends based on the position of the sun [22, 23]. Many marine animals are known to have polarization-sensitive vision, including cephalopods such as cuttlefish, squids, and octopuses, crustaceans such as fiddler crabs and mantis shrimp , and many fish [24, 25]. These animals use polarization vision for a variety of tasks, including improving visual contrast for predator or prey detection [26], communication and signaling [27, 28], and potentially for navigation [29]. Indeed, it has been hypothesized by several authors that the underwater polarization patterns contain sufficient information to perform celestial navigation without direct observation of the sun [22, 23]. As the sun-dependent patterns have been observed as deep as 200 meters [30], this is an attractive potential navigation method for underwater vehicles. However, the work performed so far has only attempted to use the polarization patterns as a compass [31].

In this work, I test the hypothesis that it is possible to determine the sun’s angular position in the sky using observations of the polarization states of underwater light. To address this hypothesis, I have created an underwater polarization video camera platform based on a bio-inspired polarization image sensor [32], including the hardware, software for live control of the camera, and software for post-processing the recorded videos. I also developed a polarimetric calibration method to correct the fixed-pattern noise caused by variations in the polarization response across the sensor [33]. Further, I have developed and tested an algorithm for inferring the sun’s apparent position from measurements made with the underwater polarization camera. My results show that it is possible to determine the sun’s position from the underwater polarization patterns, and that my system serves as a proof-of-concept for a practical navigation system based on these principles. This research introduces a new mode of underwater navigation that could enable global-scale, GPS-free operation for underwater vehicles. It also gives insight into the potential means that marine animals with polarization sensitive vision could use to perform both local and long-distance navigation.

My contributions over the course of my doctoral studies include:

- designing and fabricating a PCB to allow an FPGA to send and receive video data with the Camera Link protocol,

- developing a real-time FPGA implementation of the polarization image processing algorithms,
- evaluating the performance of the FPGA image processing algorithms against CPU and GPU implementations [34],
- fabricating several polarization image sensors, including developing a method for aligning and mounting polarization filter arrays directly on a CCD image sensor,
- developing and evaluating a calibration method for polarization image sensors [33],
- developing Python and C++ libraries for processing polarization images and videos,
- developing a Qt/C++ graphical user interface for analyzing and rendering polarization videos,
- developing and building an underwater polarization video camera platform, including:
    - hardware system design to support polarization and orientation sensors,
    - custom PCBs for interfacing with Canon EF-S lenses and the underwater housing's controls,
    - developing microcontroller software for translating the Canon lens protocol and underwater housing controls to USB,
    - and developing software for real-time control of the polarization sensor with live display of polarization video;
- and assisting collaborators with analysis of polarization images and video [35, 36].

Chapter 2 discusses the principles of polarized light and how it is mathematically modeled, sensor architectures used to image the polarization states of light, and polarization image processing techniques. Chapter 3 covers a performance analysis of various implementations of the polarization image reconstruction algorithm [34]. Chapter 4 introduces the polarimetric calibration method and quantifies the improvements it makes to the reconstructed polarization images [33]. Chapter 5 describes the hardware and software design of the underwater polarization camera. Finally, Chapter 6 covers the underwater navigation algorithm and experimental results.

Chapter 2: The Polarization of Light and Imaging Polarimeters

2.1 Polarization of Light

Transverse electromagnetic waves, such as visible light and broadcast radio waves, have three independent, fundamental properties: intensity, wavelength, and polarization. Humans readily perceive intensity and wavelength as brightness and color, respectively, but can only detect polarization through a secondary visual effect known as Haidinger's Brushes [37]. Polarization refers to the shape and orientation of the ellipse, line, or circle an electromagnetic wave traces out as it travels through space and time. Most optical events—for example reflection, refraction, and scattering—can change the polarization state of light depending on the materials involved and their geometry.

When discussing the polarization of light, we tend to use terms that describe the polarization ellipse rather than the less intuitive wave equations or Stokes parameters. As illustrated in Figure 2.1, the angle of polarization, AoP or ψ, is the angle of the ellipse's major axis relative to the x-axis, and the ellipticity, χ, is the angle of the line from the tip of the major axis to the tip of the minor axis, relative to the major axis. When $\chi > 0$, the wave is propagating with a right-handed spiral, and when negative, a left-handed spiral. When $\chi = 0°$ the ellipse degenerates into a line and we say the wave is linearly polarized; and when $\chi = \pm 45°$ the ellipse degenerates into a circle and the wave is called circularly polarized.

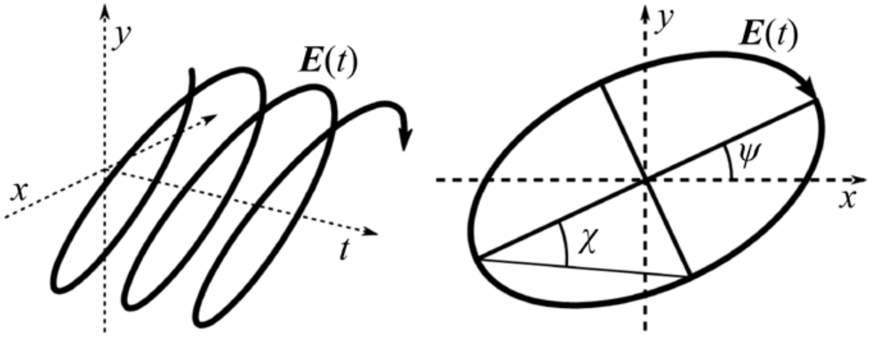

Figure 2.1 An electric field $\boldsymbol{E}(t)$ traces out the polarization ellipse over time. ψ is the polarization angle and χ is the ellipticity angle.

Another common term is the degree of polarization, DoP or p, which does not refer to the polarization ellipse but describes the average behavior of an ensemble of waves. If all of the waves in an ensemble have the same polarization state, then $p = 1$ and it is called fully polarized. However, it is common for an ensemble of waves to have varying polarization states. In this case the ensemble of waves can be decomposed by the principle of superposition into two waves of orthogonal polarization states. If the intensities of these orthogonal components are identical, then the polarization states cancel, $p = 0$, and the light is called unpolarized. Otherwise the light is partially polarized, and the DoP is the ratio of the difference in intensity between the two components over the ensemble's total intensity: $p = \left|I_{\parallel} - I_{\perp}\right|/I_{total}$.

When mathematically modelling polarized light, it is convenient to use the Mueller-Stokes representation of light and optical events. The Stokes vector,

$$\boldsymbol{S} = (S_0\; S_1\; S_2\; S_3)^T \in \mathbb{R}^4 \tag{2.1}$$

is composed of the four Stokes parameters, which are measurable intensities first described by Sir George Stokes circa 1850[1]. The first component, S_0, is the total intensity of the light. S_1 and S_2 describe the major axis of the polarization ellipse, and S_3 describes the ellipticity. The ellipse

---

[1] Many authors cite "On the change of refrangibility of light" by Sir Stokes [36] in reference to his invention of the Stokes vector, but I could find no mention of it there.

parameters and DoP are related to the Stokes parameters as per Eqs 2.2 through 2.4, illustrated by the Poincaré sphere in .

$$\tan 2\psi = \frac{S_2}{S_1} \tag{2.2}$$

$$\mathrm{Sin}\, 2\chi = \frac{S_3}{S_0} \tag{2.3}$$

$$p = \frac{\sqrt{S_1^2 + S_2^2 + S_3^2}}{S_0} \tag{2.4}$$

Note that linearly polarized light can be fully described with only S_0, S_1, and S_2, which leads to the concept of degree of linear polarization (DoLP), defined as

$$p_l = \frac{\sqrt{S_1^2 + S_2^2}}{S_0}. \tag{2.5}$$

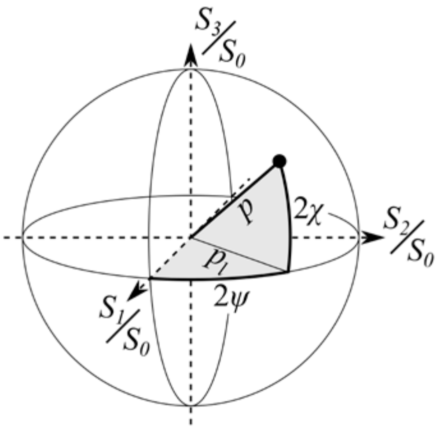

Figure 2.2 The Poincaré sphere illustrates the relationship between the Stokes vector, the polarization ellipse, and the degree of polarization.

The polarization changes caused by optical events are represented by left-multiplying the Stokes vector of the incident light by a Mueller matrix, $\mathbf{M} \in \mathbb{R}^{4\times 4}$. The matrices for complex events, such as reflections, refraction, and scattering, are often composed from the matrices of the basic polarizing elements: linear polarizers, $\mathbf{M}_P$; linear retarders, $\mathbf{M}_R$; and rotators, $\mathbf{M}_\theta$.

The Mueller matrix of a linear polarizer with the transmitting axis at 0° is

$$\mathbf{M}_P = T\begin{pmatrix} 1 & D & 0 & 0 \\ D & 1 & 0 & 0 \\ 0 & 0 & \sqrt{1-D^2} & 0 \\ 0 & 0 & 0 & \sqrt{1-D^2} \end{pmatrix}, 0 \le \{T, D\} \le 1 \qquad (2.6)$$

where T is the transmission ratio of the polarizer and D is the diattenuation. The transmission ratio and diattenuation can be intuitively understood in terms of the filter's behavior when illuminated with unpolarized light—the transmission ratio is the attenuation coefficient of the light's intensity, and the diattenuation is the DoP of the filtered light. An ideal linear polarizer has $T = 1/2$ and $D = 1$, while a neutral density filter with optical density d, which only changes intensity, would have $T = 10^{-d}$ and $D = 0$. Linear polarizers are often described by their extinction ratio as well: $R = (1 + D)/(1 - D)$.

A linear retarder with the fast axis at 0° is represented by

$$\mathbf{M}_R = \begin{pmatrix} 1 & 0 & 0 & 0 \\ 0 & 1 & 0 & 0 \\ 0 & 0 & \cos\phi & \sin\phi \\ 0 & 0 & -\sin\phi & \cos\phi \end{pmatrix} \qquad (2.7)$$

where ϕ is the retardance in radians, relative to the wavelength of the light. For example a quarter-wave retarder would have $\phi = 90°$.

Finally, a polarization rotator, which rotates the electric field vector by an angle θ in the counter-clockwise direction, is

$$\mathbf{M}_\theta = \begin{pmatrix} 1 & 0 & 0 & 0 \\ 0 & \cos 2\theta & -\sin 2\theta & 0 \\ 0 & \sin 2\theta & \cos 2\theta & 0 \\ 0 & 0 & 0 & 1 \end{pmatrix}. \qquad (2.8)$$

Note that rotating an electric field vector by θ results in rotating a Stokes vector by 2θ—this is because electromagnetic waves 180° out of phase are identical in the Stokes space. It is also common to present the transpose of this matrix as the rotator, which would correspond to rotating the coordinate system of the electric field vector rather than the vector itself. In addition to representing optical elements such as Faraday rotators and optically active materials, the rotator matrix is also used to create composite matrices that represent rotated optical elements. For example, the matrix for a rotated linear polarizer with the transmitting axis at angle θ is

$$\mathbf{M}_{P,\theta} = \mathbf{M}_{\theta}\mathbf{M}_{P}\mathbf{M}_{-\theta} \tag{2.9}$$

which uses the rotation matrix to transform the Stokes vector to and from the rotated coordinate system of the polarizer.

2.2 Imaging Polarimeter Architectures

There are many variations of polarization image sensor that operate in the visible spectrum, however all of them are based around the same measurement principle. Because the frequency of visible-spectrum electromagnetic waves is so high it is practically impossible to measure the phase (and polarization state) directly. Thus, all of the sensor designs are based on modulating the polarization state onto one or more measurable parameters of the light. In most cases, the modulated parameter is the light intensity, but sensors based on spatial and spectral modulation exist as well [39, 40]. Fully describing the polarization state of light requires three independent variables in addition to the light’s intensity. Typical applications require measuring at least two of the three polarization state parameters—if they are mixed into the same measurable quantity then a multiplexing scheme is required to separate them into different modulation channels such that the desired aspects of the polarization state can be reconstructed [41].

The most common visible-spectrum imaging polarimeter architectures are based on intensity modulation with variations on multiplexing, for example division of time (DoT), division of amplitude (DoA), and division of focal plane (DoFP) [42]. A DoT polarimeter has a single intensity image sensor with a time-varying polarization filter, often a rotating linear polarizer, as the modulating element. Reconstructing the polarization state of light requires combining images taken at different times. DoT polarimeters are simple to construct and can have very high spatial resolution, but are unsuitable for imaging dynamic scenes due to motion blur. DoA sensors, on the other hand, employ a system of beam-splitters and polarization filters to direct the image to different image sensors based on polarization state. These sensors capture all of the modulated images simultaneously so they do not suffer from motion blur, but instead they require pixel-level alignment of the sensors. The precise alignment required of the DoA sensor optics means that shocks or temperature fluctuations can introduce significant errors.

Finally, DoFP polarimeters consist of an array of a repeating pattern of different polarization filters mounted directly on the focal-plane of an image sensor [43]. Like the DoA architecture, these sensors measure all of the modulated polarization components in a single snapshot, so they avoid motion blur, but they are also compact and more physically robust because the filters are mounted directly on the sensor. The drawbacks of this architecture are that it is difficult to manufacture, it suffers a slight spatial resolution loss compared to the DoT and DoA architectures, and the periodic nature of the filter array can introduce spatial aliasing errors between the components of the polarization state [44]. Fortunately, a variety of interpolation and reconstruction methods have been developed to mitigate the resolution loss and aliasing errors [44-47].

The DoFP polarimeter architecture was suitable for the underwater video camera because of its lack of motion blur and compact, robust design. The sensors I assembled for this project consisted of Kodak/On Semiconductor KAI series CCD image sensors with 7.4 µm pixels integrated with arrays of pixel-pitch matched, aluminum nanowire, linear polarization filters. To operate in the visible spectrum, the nanowires must be significantly smaller than operating wavelength of light—in this case the filters are composed of parallel nanowires 140 nm thick, 70 nm wide, and spaced with a 140 nm pitch [48]. The filters are oriented in a repeating pattern of 0°, 45°, 135°, and 90°, shown in Figure 2.3. Each instance of the 2×2-pixel pattern is called a "super-pixel". This filter pattern allows for the reconstruction of the first three Stokes parameters, or the intensity (I), degree of linear polarization (DoLP), and angle of polarization (AoP). The characteristics of these polarimeters are thoroughly described in [49].

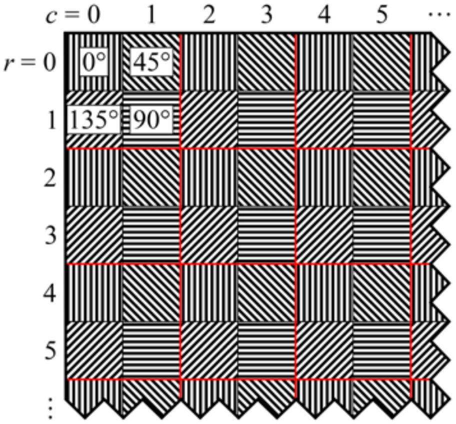

Figure 2.3 Schematic of the DoFP sensor showing the polarization filter pattern. The filters are labeled with the orientation of their transmission axis, which is perpendicular to the nanowire orientation. Each 2×2 instance of the pattern, outlined in red, is called a "super-pixel."

2.3 DoFP Polarimeter Image Processing

As stated previously, the DoFP polarimeter captures intensity images that have been modulated by the polarization state of the light. The intensity each pixel of the sensor measures can be mathematically modeled as follows:

$$I(r,c) = \begin{pmatrix}1 & 0 & 0 & 0\end{pmatrix} \cdot \mathbf{M}(r,c) \cdot \boldsymbol{S}(r,c) = \boldsymbol{A}(r,c) \cdot \boldsymbol{S}(r,c) \qquad (2.10)$$

where r and c are the row and column coordinates of the pixel, $\mathbf{M}(r,c)$ is the Mueller matrix of the pixel's polarization filter, and $\boldsymbol{S}(r,c)$ is the incident Stokes vector. The leading (1 0 0 0) vector selects the intensity component of the filtered Stokes vector; combined with $\mathbf{M}(r,c)$ it leaves just the first row of the Mueller matrix, $\boldsymbol{A}(r,c) \in \mathbb{R}^{1\times 4}$, which is called the pixel's "analysis vector."

The repeating pattern of the filters over the focal plane results in $\boldsymbol{A}(r,c)$ assuming a periodic nature as well:

$$\boldsymbol{A}(r,c) = \frac{1}{4}\begin{pmatrix} 2 \\ \cos r\pi + \cos c\pi \\ \cos r\pi - \cos c\pi \\ 0 \end{pmatrix}^T, \tag{2.11}$$

which leads to an intensity image modulated not only by the polarization state, but also over space.

$$\begin{aligned} I(r,c) &= ½S_0(r,c) + ¼(\cos r\pi + \cos c\pi)S_1(r,c) + ¼(\cos r\pi - \cos c\pi)S_2(r,c) \\ &= ½S_0(r,c) + ¼\cos r\pi\,[\mathrm{S}_1 + S_2](r,c) + ¼\cos c\pi\,[S_1 - S_2](r,c) \end{aligned} \tag{2.12}$$

A Fourier analysis of this expression reveals that the S_0 component remains centered in the spatial frequency domain, but the sum and difference of S_1 and S_2 are shifted to the Nyquist frequencies along the two spatial frequency dimensions:

$$\tilde{I}(\alpha,\beta) = ½\tilde{S}_0(\alpha,\beta) + ¼\big[\tilde{S}_1 + \tilde{S}_2\big](\alpha - ½,\beta) + ¼\big[\tilde{S}_1 - \tilde{S}_2\big](\alpha,\beta - ½), \tag{2.13}$$

where α and β are the spatial frequencies in the r and c directions, respectively. This transformation is illustrated in Figure 2.4. As Scott Tyo showed, this analysis leads to a method for perfectly reconstructing $\boldsymbol{S}(r,c)$, assuming that it is sufficiently band-limited [44]. Applying a low-pass filter isolates the S_0 component of the modulated image, while high-pass filters along r and c yield $S_1 + S_2$ and $S_1 - S_2$, respectively, from which S_1 and S_2 are trivial to compute.

Perhaps the most important result from this analysis is the identification of the spatial bandwidth limits of the DoFP architecture. Any high spatial-frequency content in intensity, in other words sharp boundaries between light and dark, will alias into false polarization signals, and *vice versa*—sharp changes in polarization state will appear in the intensity image. The cut-off frequencies of the filters used for reconstructing $\boldsymbol{S}(r,c)$ determine where such aliasing occurs, but typically one would allocate the bandwidth for each component equally at slightly less than ¼ of the total bandwidth along r and c.

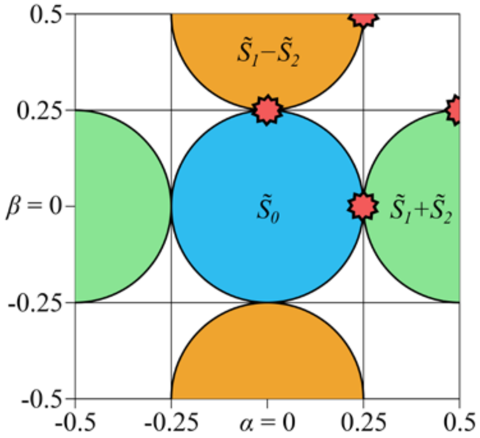

Figure 2.4 Fourier transform of the DoFP image showing how the polarization state is spatially modulated. Red stars show the location of potential aliasing when reconstruction filter cut-offs are set to ± 0.25.

While Tyo's Fourier-domain reconstruction method minimizes reconstruction errors, it is too computationally expensive for performing real-time reconstruction of polarization video. We can, however, approximate the operations from the Fourier domain with simpler spatial-domain filters. The general algorithm in this case is to separate the modulated image into 4 component images corresponding to each of the polarization filter types in the DoFP array. Then a spatial filter is used to smooth and interpolate the missing values between the pixels and the resulting images are used to reconstruct $\boldsymbol{S}(r,c)$. Indeed, much work on reconstructing polarization images from DoFP sensors has focused on the development of interpolation filters for the smoothing operation [45, 46, 50].

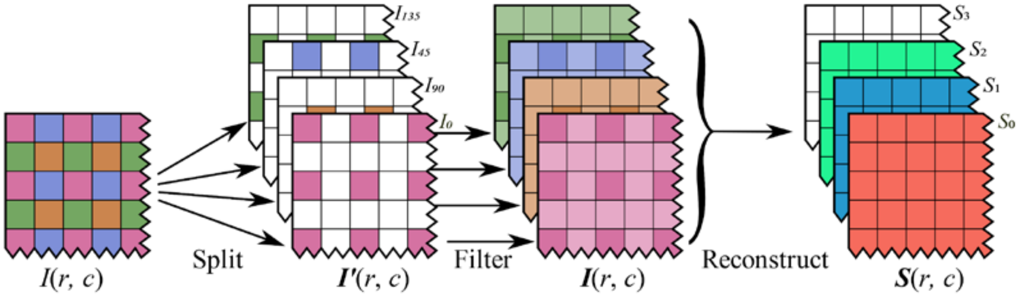

Figure 2.5 Flowchart showing the steps to reconstruct the Stokes vectors from a DoFP polarimeter image.

For any DoFP polarimeter with a 2×2 filter pattern, the split step expands the pixels of the modulated intensity image $I(r,c) \in \mathbb{R}$ into vectors $\boldsymbol{I}'(r,c) \in \mathbb{R}^4$ that are zero everywhere but have the original pixel value set in the vector element corresponding to the pixel's filter:

$$\boldsymbol{I}'(r,c) = \begin{pmatrix} \mathrm{evn}(r)\ \mathrm{evn}(c) \\ \mathrm{odd}(r)\ \mathrm{odd}(c) \\ \mathrm{evn}(r)\ \mathrm{odd}(c) \\ \mathrm{odd}(r)\ \mathrm{evn}(c) \end{pmatrix} I(r,c), \tag{2.14}$$

where $\mathrm{evn}(n) = n \bmod 2$ and $\mathrm{odd}(n) = 1 - \mathrm{evn}(n)$.

After separating the different modulated intensity channels, $\boldsymbol{I}'(r,c)$ is then filtered with an interpolation filter to fill in the missing values. For example, to match the operation of Tyo's Fourier-domain reconstruction, one would use a 2D Whittaker-Shannon sinc filter:

$$\boldsymbol{I}(r,c) = \sum_{r',c'} \boldsymbol{I}'(r',c')\, \mathrm{sinc}\frac{r-2r'}{2}\, \mathrm{sinc}\frac{c-2c'}{2} \tag{2.15}$$

where $\mathrm{sinc}\, x = \sin(x\pi)/x\pi$. However, this requires summing over the entire image to filter a single pixel. More reasonable interpolation filters, such as finite impulse response (FIR), bilinear, and bicubic filters, only operate on small regions of the image at a time, making them more tractable for real-time applications. The least computationally expensive interpolation filter is a nearest-neighbor filter, but such filters introduce large aliasing errors unless the image is severely band-limited [44]. The next simplest is the bilinear interpolation filter, which operates over a 3×3 pixel window and is defined as in [45]:

$$\boldsymbol{I}(r,c) = \sum_{i=-1}^{1} \sum_{j=-1}^{1} \boldsymbol{I}'(r+i, c+j)\, 2^{-|i|}\, 2^{-|j|}\,. \tag{2.16}$$

For sensors with the filter pattern shown in Figure 2.3, the Stokes vector for each pixel can be reconstructed as

$$\boldsymbol{S} = \begin{pmatrix} (I_0 + I_{45} + I_{90} + I_{135})/2 \\ I_0 - I_{90} \\ I_{45} - I_{135} \\ 0 \end{pmatrix}, \qquad \boldsymbol{I} = \begin{pmatrix} I_0 \\ I_{90} \\ I_{45} \\ I_{135} \end{pmatrix}. \tag{2.17}$$

More generally, the analysis vectors of the filters can be used to generate a reconstruction matrix:

$$\boldsymbol{S}(r,c) = \mathbf{A}^{-1} \cdot \boldsymbol{I}(r,c), \qquad \mathbf{A} = \begin{pmatrix} \boldsymbol{A}(0,0) \\ \boldsymbol{A}(1,1) \\ \boldsymbol{A}(0,1) \\ \boldsymbol{A}(1,0) \end{pmatrix}. \tag{2.18}$$

Finally, in addition to reconstructing the Stokes vector, it is useful to compute the AoP image, $\psi(r,c)$, and the DoP or DoLP image, $p(r,c)$ or $p_l(r,c)$, following Eqs. 2.2 to 2.5, as they are easier for people to interpret and understand. Typically, these images are shown in false color, AoP by mapping 2ψ to the hue wheel, and DoP by mapping p to a contrast-enhancing color gradient, though more sophisticated visualization schemes are in use as well [51].

Chapter 3: DoFP Image Processing Performance Comparison

This chapter contains material from “A comparison of polarization processing across different platforms” published in the Proceedings of SPIE Volume 8160, 2011 [34].

Several implementations of the DoFP image processing algorithm were tested for performance in terms of latency, throughput, output accuracy, and power consumption. This study was performed in collaboration with Timothy York, who was responsible for programming the CPU and GPU implementations. I programmed the FPGA implementation and set up the power measurement hardware, analysis of the results and preparation of the manuscript was shared between us.

3.1 Algorithm Implementations

The specific algorithm tested was as shown in Figure 2.5, specifically with the 3×3 bilinear interpolation of Equation 2.15, and with the addition of a calibration scheme before the interpolation step. For this study, the pixel intensity responses were calibrated by

$$I_{cal}(r,c) = \big(I(r,c) - d(r,c)\big) \cdot g(r,c) - \hat{S}_0\big(\lfloor r/2 \rfloor, \lfloor c/2 \rfloor\big) \cdot c(r,c), \qquad (3.1)$$

where d is the pixel’s dark-value, and g and c are per-pixel calibration coefficients. $\hat{S}_0$ is an estimate of the intensity of each super pixel, computed as

$$\hat{S}_0\big(\lfloor r/2 \rfloor, \lfloor c/2 \rfloor\big) = \sum_{i=r}^{r+1} \sum_{j=c}^{c+1} g(i,j)\, I(i,j)\,. \qquad (3.2)$$

The derivation of these equations and the values of their parameters will not be covered as this calibration method has since been superseded by the algorithm described in Chapter 4.

The algorithm was implemented on 3 platforms for testing: a general-purpose multi-core CPU, an Nvidia GPU, and an FPGA. The CPU implementation was written in C++, and was broken up into a series of three tasks: calibration (Eqs. 2.19 and 2.20), interpolation (Eqs. 2.14 and 2.16), and reconstruction (Eqs. 2.17, 2.2, and 2.5). The reconstruction task also included converting the AoP image to false-color. Each task was written as a single function that operates on an entire frame of data at once, iterating over the image in row-major order using two nested loops. This serial implementation is used as the reference for benchmarking all of the other implementations. To take advantage of the multiple cores and SMT capabilities of modern CPUs, the algorithm was multithreaded using two methods. The first uses OpenMP, an API for shared-memory parallel programming, to distribute the iterations of the outer loop of each task across multiple threads. OpenMP automatically sets the number of threads to make the best use of the CPU's multiple cores and SMT capabilities [52]. The second method pipelines each input frame into a separate thread so that multiple frames are processed at the same time. The number of threads used is set to match the CPU's capabilities. The two parallelization schemes are compared to the serial algorithm in Figure 3.1. Each of the parallelized versions was implemented using both single and double precision floating point arithmetic to compare the accuracy/speed trade-off.

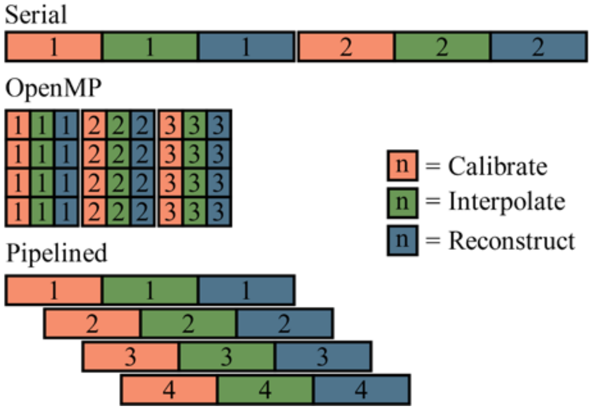

Figure 3.1 CPU parallelization schemes for the DoFP image processing algorithm.

The Nvidia GPU implementation was written using the CUDA C/C++ extensions [53]. The computations are the same as the reference CPU implementation, but are broken into two kernels which run concurrently on all pixels, subject to thread scheduling. The first kernel implements the calibration algorithm. The second kernel implements the rest of the processing flow. Since each kernel is run simultaneously on every pixel, the separation enforces that calibration finishes before interpolation begins. The GPU version was also implemented using both single and double precision arithmetic.

Finally, the image processing algorithm was implemented on a Xilinx Virtex-5 FPGA using the Verilog language. Several modifications were made to accommodate the FPGA hardware. First, the calculations are all performed using fixed-point operations rather than floating point. Second, the CORDIC algorithm is used to compute $\sqrt{S_1^2 + S_2^2}$ and $\arctan S_2/S_1$ for the AoP and DoLP images [54]. And finally, the calibration algorithm was simplified to only applying a per-pixel gain and a constant offset as there was insufficient memory on the platform to hold all of the coefficients use in the full calibration algorithm.

The FPGA implementation uses a streaming, fully pipelined architecture that takes in a raw pixel and outputs a processed pixel every clock cycle. A block diagram is shown in Figure 3.2.The first stage of the pipeline performs calibration. Its output streams into a delay stage that outputs the current pixel and the corresponding pixel from the two previous rows of the image. These are required for the bilinear interpolation stage which operates on a 3×3-pixel window of the calibrated image. The stream of interpolated pixels feeds into stage which computes the intensity, DoLP, and AoP: S_0, p_l, and ψ. Finally, a multiplexer selects which of these data streams will be sent to the PC for display.

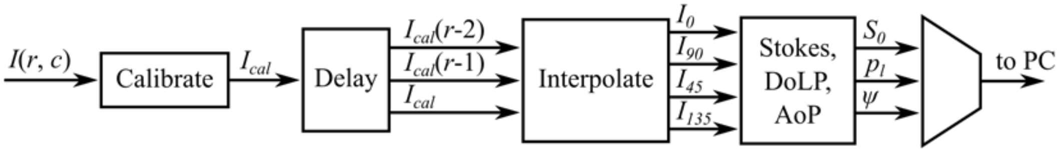

Figure 3.2 Block diagram of the FPGA implementation.

3.2 Performance Comparison

The PC used for measurement is a 2.93 GHz Intel Core i7-940, with 12 GB of PC3 12800 RAM and an Nvidia GTX 480 GPU. The measurements for the CPU and GPU implementations were taken by capturing a 768-frame video from the polarization sensor. Due to sampling limitations with the multimeters, the video was divided into 24-frame segments. The segments were processed, and a per-frame time was taken using the Windows system call QueryPerformanceCounter. The total time was taken as well. Processing the video was repeated 10 times, and the average throughput, measured as the total time to compute all frames divided by the number of frames, was computed. The average latency was computed as the average time per frame.

The power consumption was measured using two Agilent 34410A digital multimeters and an Agilent 33220A function generator. The function generator outputs a trigger simultaneously to both multimeters at the start of processing using the VISA library. As shown in Figure 3.3, one multimeter measures the line voltage (nominally 120 V at 60 Hz), while the other measures the voltage drop across a 0.2 Ω, 5 W series resistor to indirectly measure the current. This was done because the current was greater than the multimeter's measurement limit. Both voltages were sampled at 100 μs, and 50,000 samples were taken. Since the triggering was simultaneous, the instantaneous power was computed by multiplying the line voltage by the voltage read across the resistor divided by 0.2.

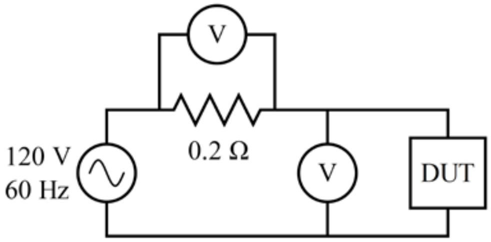

Figure 3.3 Power measurement schematic.

Since all implementations required a PC for display, the RMS power consumption of the PC was measured while the PC was idle. This is considered the baseline and was 167 W. The RMS value of the power of each trial was computed by taking the square root of the square of a moving average filter that spans six power cycles. Plots of typical RMS power measurements are shown in Figure 3.4. The plots start with the CPU in idle and processing starts ½ second into the measurements. The serial implementation does not finish before the end of these plots, however the other implementations show the dip in power as the CPU returns to idle when the processing finishes. The GPU implementation shows a higher power consumption during the idle time due to the CUDA libraries being initialized.

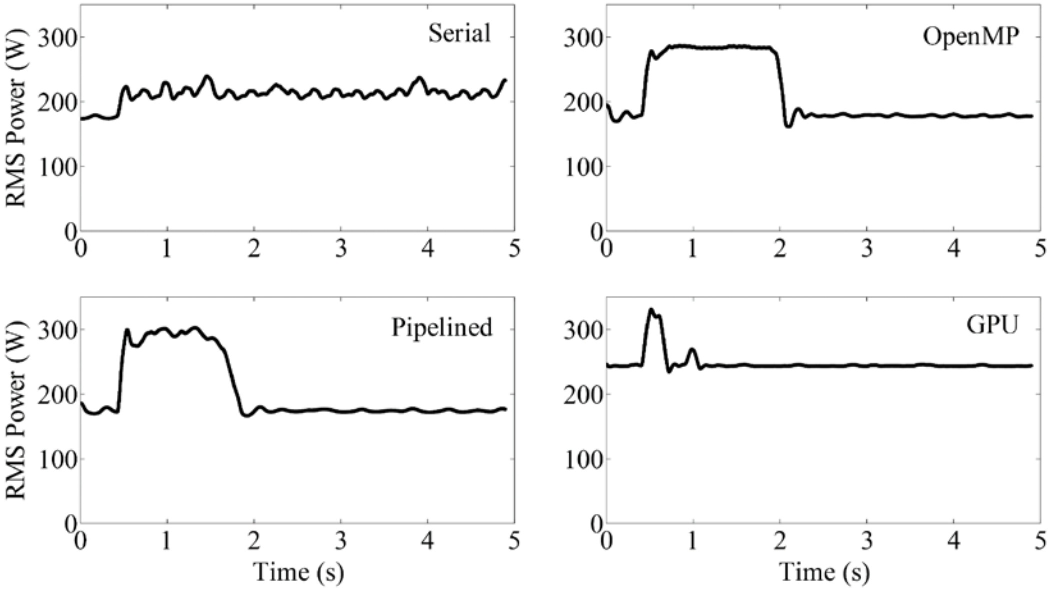

Figure 3.4 Plots of typical power usage during execution.

Implementation	Precision	Throughput	Latency	Power	Energy / frame
Reference	Double	4.10 fps	243 ms	46.1 W	11,255.7 mJ
OpenMP	Double	16.29 fps	61.5 ms	114.6 W	7,038.8 mJ
OpenMP	Single	18.92 fps	54.8 ms	107.9 W	5700.8 mJ
Pipeline	Double	19.72 fps	370 ms	104.5 W	5300.6 mJ
Pipeline	Single	22.63 fps	322 ms	117.3 W	5185.3 mJ
GPU	Double	117.66 fps	8.5 ms	142.3 W	1209.4 mJ
GPU	Single	**194.46 fps**	5.14 ms	130.8 W	672.5 mJ
FPGA	Fixed	50.00 fps	**11.4 µs**	**2.445 W**	**48.9 mJ**

Table 3.1 Implementation performance. The best values are bolded.

The RMS power curves were measured 320 times per implementation. The baseline power was subtracted from each curve, and the area under the resultant curve during the processing time was computed. This yielded the total energy consumed per frame, as reported in Table 3.1, which also lists the average power consumption during processing.

The accuracy of each implementation was measured by comparing its S_0, p_l, and ψ images to those of the reference implementation. The raw input image was randomly generated and processed without calibration by all implementations. The RMS error (RMSE) was computed by taking the square root of the mean of the squared difference image, using double precision math.

Platform	Implementation	S_0 RMSE	p RMSE	ψ RMSE
CPU	Precise double	0	0	0
CPU	Precise single	0.0083	8.743×10^{-7}	1.031×10^{-5}
CPU	Fast single	0.0083	8.743×10^{-7}	1.031×10^{-5}
GPU	Fast double	0	2.514×10^{-8}	2.188×10^{-6}
GPU	Fast single	0.0084	5.9×10^{-7}	1.04×10^{-5}
FPGA	Fixed	0	0.0238	0.0252

Table 3.2 Computational accuracy.

Of the CPU-only implementations, serial computation performed the worst, as expected. Using OpenMP to parallelize the computation quadrupled the frame rate, while pipelining garnered the best performance. The main tradeoff between the two is latency. The pipelined computation suffers from high latency as it requires the same time as a serial implementation, plus thread overhead, before a frame is computed. The multithreaded OpenMP version reduces latency by utilizing threads to compute multiple pixels at the same time. In both cases, single precision proved to be considerably faster than double precision. We believe this to be due to greater cache coherency as a result of the smaller data type.

Of the remaining implementations, the GPU implementation using single-precision is the top performer in terms of frame-rate. It is nearly four times as fast as the FPGA, and roughly nine times as fast as the pipelined CPU implementation. The main disadvantage is higher power consumption than either the CPU or FPGA, though the energy required per frame is lower than the CPU implementations. The FPGA maintains real-time speeds as well, operating at 50 frames-per-second, over twice as fast as the fastest CPU implementation, and has latency 451 times lower than the GPU and 4807 times lower than the CPU. The disadvantage of the FPGA is the loss of accuracy due to the use of the CORDIC algorithm for computing the DoLP and AoP.

In terms of form factor, the CPU implementation can run reasonably well on a high-powered laptop or small form-factor PC. The GPU has essentially the same form factor as the CPU. The FPGA implementation fits on a 2×2.5×4-inch space, but requires an external PC for control and display.

The computation required to maintain a high frame rate is challenging, even for a multi-core PC. A GPU implementation has the highest frame-rate, but also the highest power consumption. The FPGA provides a real-time frame rate and low power consumption, but at the expense of accuracy for the DoLP and AoP.

Chapter 4: DoFP Polarimeter Calibration

This chapter contains material from "Calibration methods for division-of-focal-plane polarimeters" published in Optics Express volume 21, issue 18 [33].

The polarization reconstruction method presented in Section 2.3 assumes that all of the sensor's pixels have ideal polarization filters and perfectly measure the light intensity—however this is far from the case. Fixed pattern noise (FPN), referring to constant spatial variations in pixel response, is a common source of error on any image sensor. In typical sensors, the FPN is due to small variations in transistor sizes and doping levels in the photodiodes and read-out amplifiers across the focal plane array [55, 56]. Techniques such as correlated double sampling and difference double sampling effectively correct the FPN caused by these variations in the sensor's electronics [55, 56]. DoFP polarimeters, however, also have FPN caused by spatial variations in the polarization filter array. The polarization filters, as mentioned previously, consist of parallel aluminum nanowires with nominal dimensions of 140 nm thick by 70 nm wide, and are spaced with a 140 nm pitch. However, the true dimensions can vary by as much as 20 nm [57, 58]. Such variations have a major impact on the optical performance of a nanowire filter [59], in fact spatial variations in polarization properties up to 20% have been reported for a DoFP polarimeter with nanowire filters [49]. Using more advanced manufacturing techniques can reduce the nanowire variation and reduce this source of FPN, but it would also lead to prohibitively expensive filters and imaging devices. Thus, this work explores using computational methods for correcting the variations in polarization response over the pixels of a DoFP polarimeter.

4.1 Calibration Function Derivation

The pixel model used to derive the polarimeter calibration functions is based on Eq. 2.10, but with the addition of a pixel dark-offset:

$$I = \boldsymbol{A} \cdot \boldsymbol{S} + d, \tag{4.1}$$

where $\boldsymbol{A} \in \mathbb{R}^{1\times 4}$ is the pixel's analysis vector, $\boldsymbol{S} \in \mathbb{R}^4$ is the incident light's Stokes vector, and d is the pixels dark value. Since we are interested in the FPN components introduced by the polarization filters, we assume that the pixel is linear and neglect any temporal or quantization noise.

When considering a "super-pixel", the responses of the n constituent pixels are stacked into a column vector $\boldsymbol{I} \in \mathbb{R}^4$:

$$\boldsymbol{I} = \begin{pmatrix} \boldsymbol{A}_1 \cdot \boldsymbol{S} + d_1 \\ \vdots \\ \boldsymbol{A}_n \cdot \boldsymbol{S} + d_n \end{pmatrix} = \begin{pmatrix} \boldsymbol{A}_1 \\ \vdots \\ \boldsymbol{A}_n \end{pmatrix} \boldsymbol{S} + \begin{pmatrix} d_1 \\ \vdots \\ d_n \end{pmatrix} = \mathbf{A} \cdot S + \boldsymbol{d}\,. \tag{4.2}$$

The individual analysis vectors and dark offsets are combined into an analysis matrix, $\mathbf{A} \in \mathbb{R}^{4\times 4}$, and a dark offset vector, $\boldsymbol{d} \in \mathbb{R}^4$. This model assumes that either the incident illumination is uniform across the super-pixel or that all of the constituent pixels are co-located.

The purpose of a calibration function is to transform the non-ideal response of a pixel or super-pixel into the ideal response. In the ideal response, the dark values are zero and the analysis vectors match their nominal values—in our case specified by Eq. 2.11. Because the pixel model is linear, this can be expressed by basic linear transformations. In the single-pixel case,

$$I_c = g_c(I - d_c) \approx \boldsymbol{A}_i \cdot \boldsymbol{S} \tag{4.3}$$

where I_c is the calibrated pixel value, $\boldsymbol{A}_i$ is the pixel's nominal analysis vector, and g_c and d_c are the calibration gain and offset, respectively. In the super-pixel case, the calibration function is

$$\boldsymbol{I}_c = \mathbf{G}_c(\boldsymbol{I} - \boldsymbol{d}_c) \approx \mathbf{A}_i \cdot \boldsymbol{S} \tag{4.4}$$

where as in the single-pixel case, $\mathbf{A}_i$ is the nominal analysis matrix of the super-pixel, $\mathbf{G}_c \in \mathbb{R}^{4\times 4}$ is the calibration gain matrix and $\boldsymbol{d}_c \in \mathbb{R}^4$ is the calibration offset vector.

The values of the calibration gains and offsets can be found by expanding Eqs. 2.23 and 2.24 with the pixel and super-pixel models, respectively, and minimizing the squared error between the calibrated response and the nominal response:

$$\min\|g_c(\boldsymbol{A}\cdot\boldsymbol{S}+d-d_c)-\boldsymbol{A}_i\cdot\boldsymbol{S}\|^2\,, \tag{4.5}$$

$$\min\|\mathbf{G}_c(\mathbf{A}\cdot\boldsymbol{S}+\boldsymbol{d}-\boldsymbol{d}_c)-\mathbf{A}_i\cdot\boldsymbol{S}\|^2\,. \tag{4.6}$$

Both minimizations are convex and can be completed by taking the partial derivatives with respect to the calibration gains and calibration offsets, setting them to zero, and solving for the parameters. It is also possible to solve for the calibration parameters numerically by supplying measured pixel responses to illumination with known $\boldsymbol{S}$ values to an ordinary least-squares solver.

A solution to Eq 2.25, the single pixel case, is

$$d_c=d,\qquad g_c=\frac{\boldsymbol{A}_i\cdot\boldsymbol{S}}{\boldsymbol{A}\cdot\boldsymbol{S}}. \tag{4.7}$$

The calibration dark offset is set to the pixel’s dark offset and the calibration gain is the ratio of the two projections. When substituted back into Eq. 2.23,

$$I_c=\frac{\boldsymbol{A}_i\cdot\boldsymbol{S}}{\boldsymbol{A}\cdot\boldsymbol{S}}(\boldsymbol{A}\cdot\boldsymbol{S}+d-d)\approx\boldsymbol{A}_i\cdot\boldsymbol{S}, \tag{4.8}$$

we see that the dark offset is completely corrected, but the calibration gain only rescales the projection of $\boldsymbol{S}$ onto $\boldsymbol{A}$ to the same length as the projection of $\boldsymbol{S}$ onto $\boldsymbol{A}_i$. This only results in the nominal pixel response if $\boldsymbol{A}$ is a scalar multiple of $\boldsymbol{A}_i$, in other words this method can only correct for variations in the filter transmission ratio, not variations in diattenuation, polarization angle, or ellipticity.

A solution to the super-pixel case, Eq. 2.26, is

$$\boldsymbol{d}_c=\boldsymbol{d},\qquad \mathbf{G}_c=\mathbf{A}_i\mathbf{A}^{+}. \tag{4.9}$$

where $\mathbf{A}^{+}$ indicates the pseudo-inverse of $\mathbf{A}$, which is computed such that $\mathbf{G}_c\mathbf{A} = \mathbf{A}_i$ is satisfied. As long as the pseudo-inverse exists, $\mathbf{G}_c$ will transform each pixel's analysis vectors, by scaling and rotating, into exactly their nominal values. Eq. 2.30 shows that using this approach perfectly calibrates the polarization response as long as the model's assumptions hold.

$$\mathbf{G}_c(\boldsymbol{I} - \boldsymbol{d}_c) = \mathbf{A}_i\mathbf{A}^{+}(\mathbf{A} \cdot \boldsymbol{S} + \boldsymbol{d} - \boldsymbol{d}) = \mathbf{A}_i\boldsymbol{S} \tag{4.10}$$

4.2 Calibration Function Evaluation

4.2.1 Experimental Setup

The two calibration functions presented in Eqs. 2.23 and 2.24 were evaluated on data collected from the apparatus shown in Figure 4.1. A Sylvania EHJ64655HLX 250 W tungsten-halogen bulb provides light for the system. The light passes through an Edmund Optics Heat Absorbing Glass to block unwanted IR components, then optionally through 1 of three narrow-band spectral filters: Thorlabs FB450-10, Newport 10LF10-515, or Thorlabs FB600-10, which pass 450, 515 and 600 nm light, respectively. An adjustable shutter controls the light intensity to avoid any spectral variations caused by changing the current through the lamp. The light then passes into a 4" integrating sphere which produces nominally uniform, unpolarized light at its outputs. A Thorlabs S120VC calibrated photodiode placed at one output port of the integrating sphere measures relative light intensities. Light from the other output port passes through a Newport 20LP-VIS-B linear polarizer mounted on a motorized rotation stage, and finally passes into the visible-spectrum, linear, DoFP polarimeter described in [49, 60]. The apparatus generates fully linearly polarized light with arbitrary intensity and polarization angle. It can be switched between "white" light directly from the lamp or one of several narrow-band spectra provided by the spectral filters. Since the polarimeter being used for evaluation only measures linear polarization there is no need for circularly polarizing optics. The capability to control the degree of linear polarization will be included for future works.

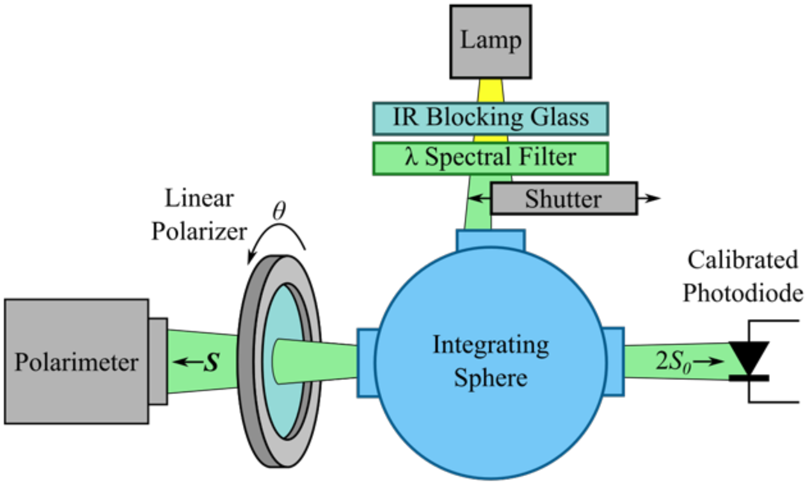

Figure 4.1 Polarization state generator for evaluating calibration techniques.

Polarization images were collected with unfiltered, 450 nm, 515 nm, and 650 nm light respectively. For each spectrum, 100 images at 6 different intensities and 36 polarization angles were collected from a 300×300-pixel (2.22 mm square) region of the polarimeter. The small region was selected to maximize the uniformity of the incident light and to limit the amount of data collected. The coefficient of variation of a non-polarimetric image taken over the same area was 0.0106, which will contribute to the final reconstruction errors. Each intensity and polarization angle was sampled 100 times to reduce the effects of temporal noise on the final results. The 6 intensities followed a roughly exponential sequence based on the dynamic range of the polarimeter. For each wavelength, the maximum intensity was set as high as possible without saturating any pixels at any angle of the polarizer. The remaining intensities were set at 50%, 25%, 10%, 5%, and 2.5% of the maximum intensity at each wavelength. This procedure minimized the effects of wavelength-dependent intensity variations of the photodiode’s quantum efficiency. The 36 different polarization angles were uniformly distributed every 5° from 0° to 180°, which covers the full range of linear polarization angles. The output of the integrating sphere was 3% linearly polarized, which is easily compensated for as shown in the following section. Only the images taken with white (unfiltered) light and polarization angles every 20°

were used as training data to determine the calibration parameters. The remainder of the data was used for testing the performance of the calibration procedures.

4.2.2 Determining model and calibration parameters

The first step in computing the calibration parameters of the sensor is to determine the model parameters for each pixel. The analysis vector and dark offset for each of the n pixels can be determined simultaneously from the m training data images by solving

$$\begin{pmatrix} I_{1,1} & \cdots & I_{1,m} \\ \vdots & \ddots & \vdots \\ I_{n,1} & \cdots & I_{n,m} \end{pmatrix} = \begin{pmatrix} \boldsymbol{A}_1 & d_1 \\ & \vdots & \\ \boldsymbol{A}_n & d_n \end{pmatrix} \begin{pmatrix} \boldsymbol{S}_1 & \cdots & \boldsymbol{S}_m \\ 1 & & 1 \end{pmatrix}, \qquad (4.11)$$

$$\begin{pmatrix} \boldsymbol{A}_1 & d_1 \\ & \vdots & \\ \boldsymbol{A}_n & d_n \end{pmatrix} = \begin{pmatrix} I_{1,1} & \cdots & I_{1,m} \\ \vdots & \ddots & \vdots \\ I_{n,1} & \cdots & I_{n,m} \end{pmatrix} \begin{pmatrix} \boldsymbol{S}_1 & \cdots & \boldsymbol{S}_m \\ 1 & & 1 \end{pmatrix}^{+}. \qquad (4.12)$$

The values of $\boldsymbol{S}$ must include all of the polarization effects of the apparatus, including the polarization of the output of the integrating sphere. Eq. 2.32 was evaluated using a least-squares solver. The coefficients of determination, R^2, for all of the pixels were above 99.73% and have a median of 99.93%. This indicates that the model explains most of the variation in the training data.

The pixel dark offsets are summarized in Figure 4.2. The dark offsets are small compared to the dynamic range of the polarimeter (maximum digital value of 4096), but are predominantly negative. This is not a problem, but indicates that the dark offsets are being over-corrected within the polarimeter hardware.

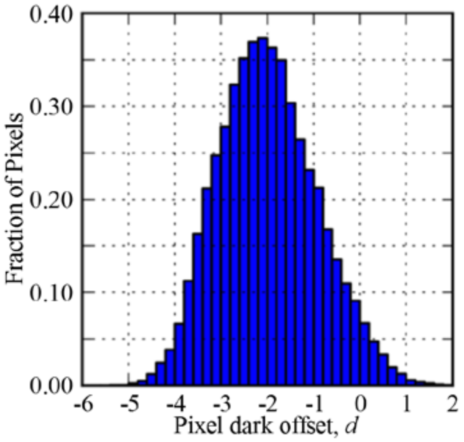

Figure 4.2 Histogram of pixel dark offsets. The digital value range for each pixel in the polarimeter is 0 to 4095, inclusive.

Figure 4.3 displays the measured analysis vectors, $A = (A_0\ A_1\ A_2\ A_3)^T$, for each pixel. Since these measurements are from pixels with linear polarization filters, A_3 is always zero and is not included. The spatial variation of the filter transmission ratios is about 20% and can be completely attributed to variations in the nanowire dimensions. The measurements show a constant angular offset of approximately 5° from nominal, which is most likely due to alignment errors during the interference lithography step of the filter fabrication [57]. Most of the filters have diattenuations of about 0.9, which corresponds to an extinction ratio of 26 dB. This is less than the values reported in [60] and is attributed to the increased cross-talk due to the lack of collimation in this work's optical apparatus. Variance in the diattenuation, however, is also attributed to manufacturing flaws in the nanowire filters. It is worth noting that any cross-talk effects are measured as part of the pixels' polarization parameters—this means that any calibration parameters derived from these measurements will be dependent on the incident light-beam's divergence and the parameters must be remeasured for imaging optics with significantly different f-numbers.

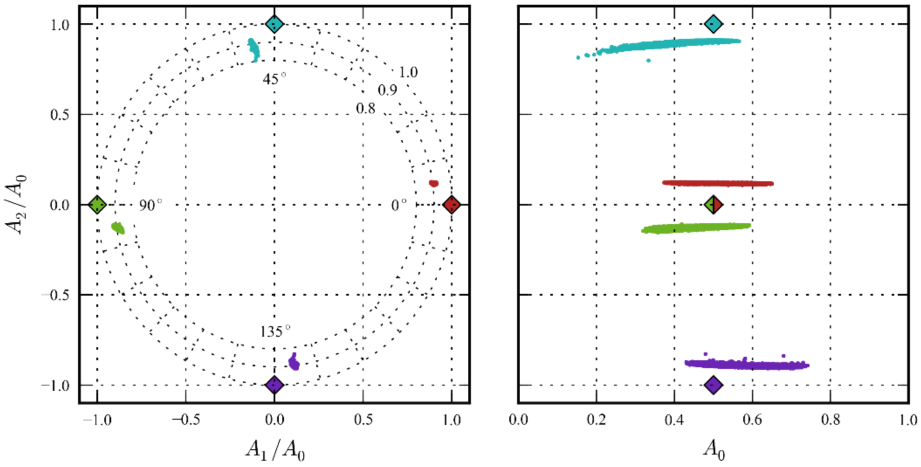

Figure 4.3 Analysis vectors, $\boldsymbol{A}$, for all pixels in the imaging array. Diamonds indicate nominal values for each colored group—red is 0°, green is 90°, blue is 45°, and purple is 135°. The ratios of A_2/A_0 versus A_1/A_0 for each pixel are presented in the left sub-plot, where the radius corresponds to a filter's diattenuation and the polar angle corresponds to its orientation. The corresponding values of A_0, the filters' transmission coefficients, are plotted along the x-axis in the right subplot.

With the analysis vector and dark offset determined for each pixel, computing the single-pixel and super-pixel calibration parameters requires following Eqs. 2.27 and 2.29 for each pixel and super-pixel, respectively. To illustrate the capabilities of the two methods, the analysis vectors are shown transformed by the calibration gains in Figure 4.4 and Figure 4.5. That is, Figure 4.4 shows $g_c\boldsymbol{A}$ for each pixel, and Figure 4.5 shows $\mathbf{G}_c\boldsymbol{A}$ for each pixel. The single-pixel calibration normalizes the length of each pixel's $\boldsymbol{A}$-vector, which reduces the transmission ratio variation to about 2%, but does not correct the diattenuation or orientation. On the other hand, the super-pixel calibration completely transforms the $\boldsymbol{A}$-vectors to their nominal transmission ratio, diattenuation, and orientation. The transmission ratio variation is less than 0.1% across the DoFP array after the super-pixel calibration is applied.

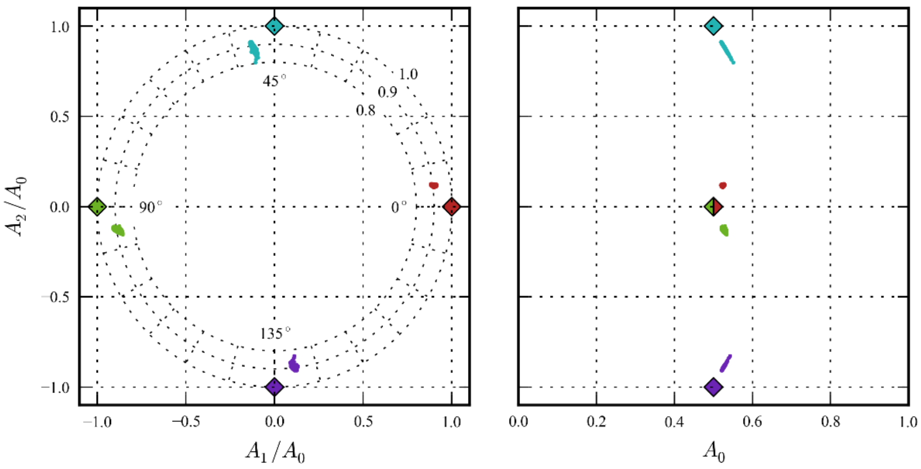

Figure 4.4 Pixel analysis vectors corrected by the single-pixel calibration gain, $g_c\boldsymbol{A}$, plotted as in Figure 4.3. The lengths of the vectors are normalized, but their orientations and diattenuations remain uncorrected.

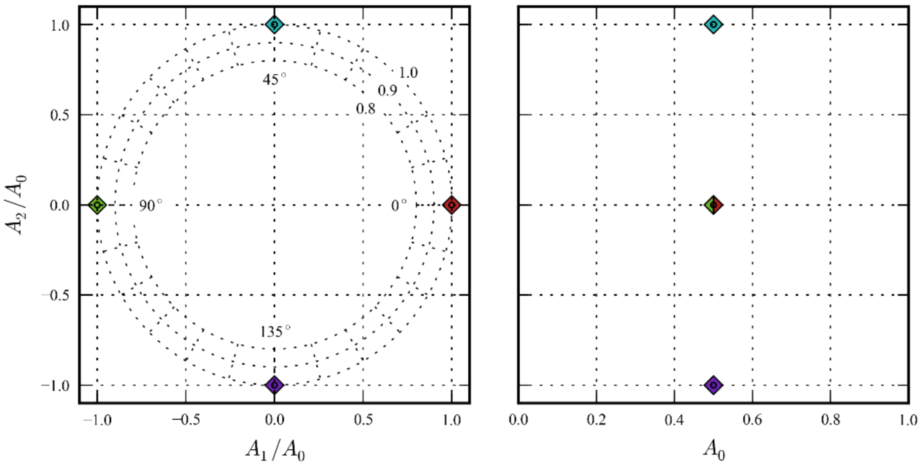

Figure 4.5 Pixel analysis vectors corrected by the super-pixel calibration gain, $\mathbf{G}_c\boldsymbol{A}$, plotted as in Figure 4.3. The vectors are transformed completely to their nominal values.

4.2.3 Calibration test results

The difference between the single- and super-pixel calibration methods is also evident when the functions are applied to the test data. Figure 4.6 and Figure 4.7 show histograms of the pixel responses when uncalibrated and with each of the two methods. The polarimeter is illuminated with linearly polarized white light at an incident angle of 15°. In Figure 4.6, the left sub-plot shows the histogram response of just the nominally 0° pixels before and after the two calibration methods are applied. The right sub-plot shows the response of all pixels when uncalibrated. The

FPN of the uncalibrated 0° pixels is 11.6% (computed as the standard deviation over the mean). In comparison, the FPN of the CCD before depositing the nanowire polarization filters was 0.5%. Applying the single- and super-pixel calibration methods reduces the FPN for the 0° pixels to 0.15% and 0.11% respectively. Figure 4.7 shows the histograms of all of the pixels after the two calibration methods—single-pixel in the left panel and super-pixel in the right. While both methods significantly reduce the variance, the super-pixel method also adjusts the pixel responses so that they are centered on their nominal values.

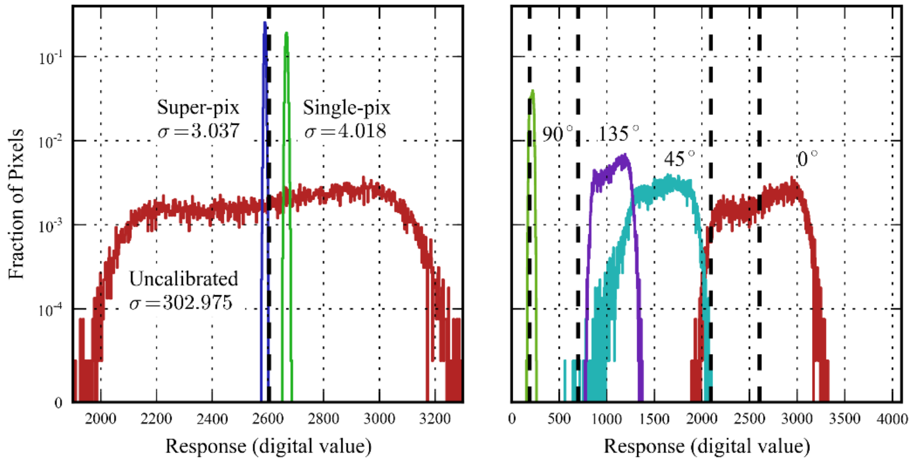

Figure 4.6 Pixel response histograms with white light at 100% intensity and linearly polarized at 15°. Left: 0° pixels with and without calibration. Right: All pixel orientations, uncalibrated.

Figure 4.8 examines the pixel responses to varying polarization angles with and without calibration. All of the responses follow Malus's squared cosine law, but when uncalibrated the amplitudes of the cosine responses vary widely, do not reach zero at their minima, and the maxima do not occur at the nominal filter angles. The single-pixel calibration method corrects the amplitude variation, but does not shift the minima to zero or adjust the phase of the cosine. The super-pixel method, however, does correct these issues as well, which is critical for accurate reconstruction of the Stokes vector.

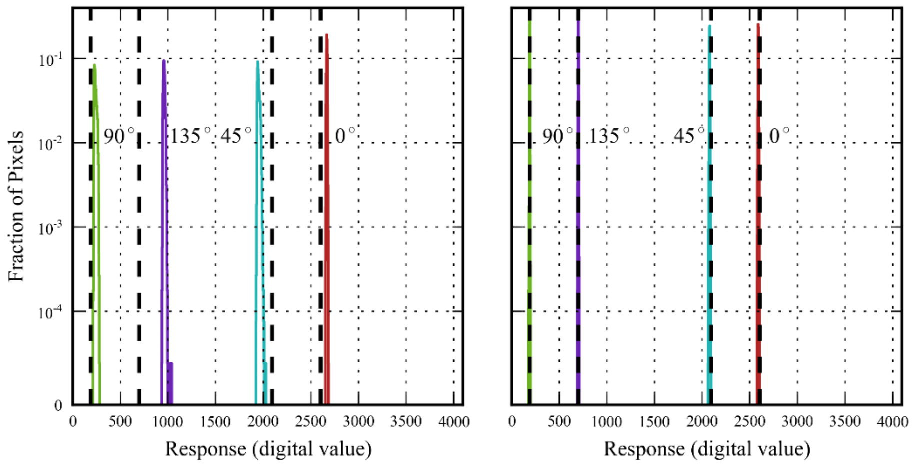

Figure 4.7 As Figure 4.6-right. Left: single-pixel calibrated. Right: super-pixel calibrated.

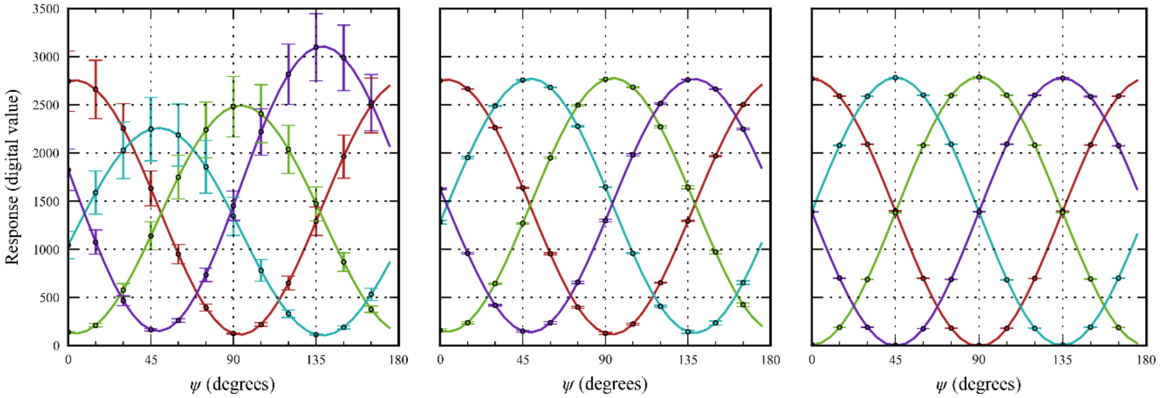

Figure 4.8 Pixel responses with white light, 100% intensity, and varying polarization angle ψ. Error bars are at ±1 standard deviation. From left to right: uncalibrated, single-pixel calibrated, super-pixel calibrated.

Figure 4.10, Figure 4.11, and Figure 4.12 show the RMS reconstruction errors of the incident intensity, DoLP, and AoP, respectively, as the incident AoP and intensity are swept through their ranges. The reconstruction errors for the uncalibrated responses show large dependencies on the incident angle of polarization. In the uncalibrated case, the maximum RMSE of the DoLP at maximum illumination is 20%, at minimum illumination it rises to 35%. The single-pixel calibration method removes most of the dependency on the incident AoP, and reduces the DoLP RMSE to 10% at maximum illumination and 32% at minimum illumination. The super-pixel calibration method further reduces these errors to 0.5% and 26% at maximum and minimum illumination, respectively. At low light levels, neither calibration method provides much error correction, however these errors are not due to FPN, but rather temporal noise—as the incident intensity drops, the pixel's thermal noise dominates and drastically decreases the pixel's signal to noise ratio. For example, using the sensor's specifications, we estimate that at 10% illumination photon shot noise accounts for 84% of the noise power and thermal noise for 16% [61]. However, a thorough noise analysis of the reconstruction algorithm would be required to determine how much the temporal noise sources contribute to the final reconstruction errors. The reconstruction errors do not reach zero, even at higher light levels, for several reasons. Of course, there is still temporal noise in the measurements even if it is reduced by averaging many frames. Additionally, the non-uniformity of the flat-field produced by the integrating sphere limits the accuracy of the measurements of the pixel polarization parameters. The measurement errors in turn propagate to the calibration parameters. And finally, the sensor's specifications indicate that the pixel responses may have non-linearities up to 2%, which is not included in our model.

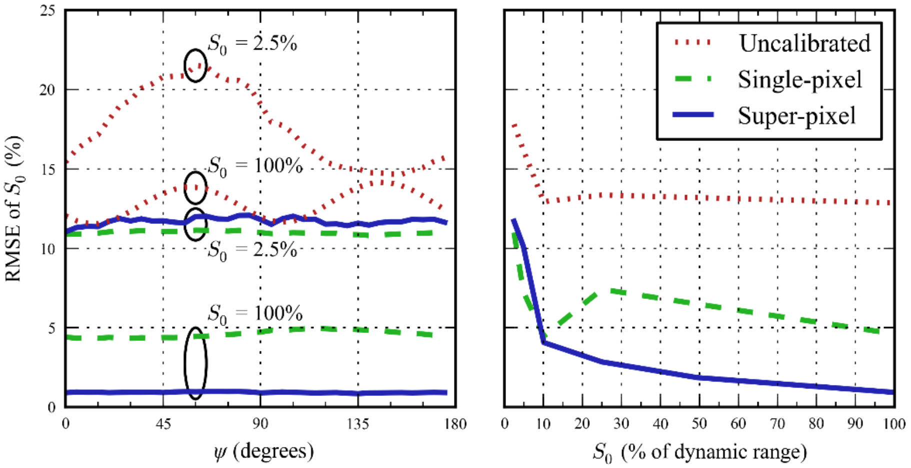

Figure 4.9 RMS error of S_0, the reconstructed light intensity, as a function of incident polarization angle, ψ, left, and of incident intensity, S_0, right.

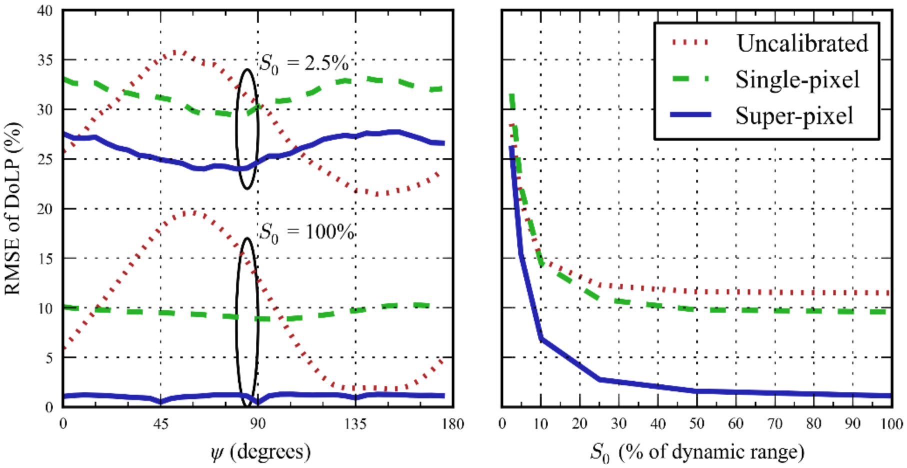

Figure 4.10 RMSE of the reconstructed DoLP as a function of incident polarization angle, ψ, left, and of incident intensity, S_0, right.

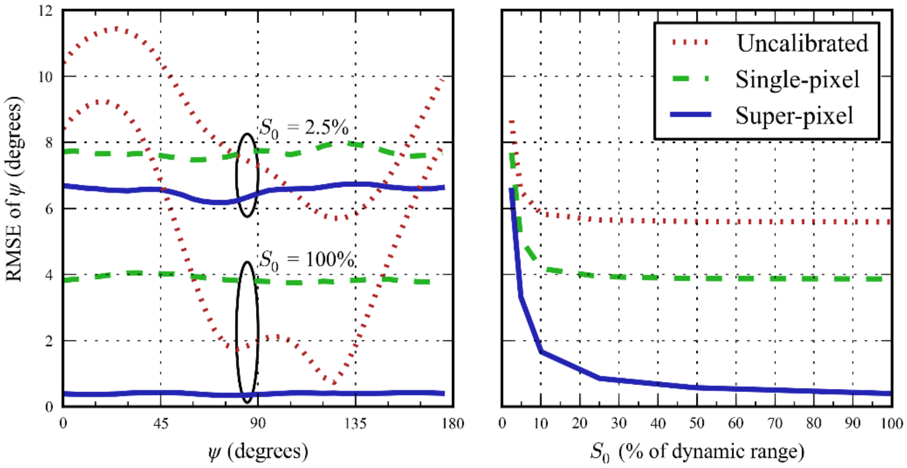

Figure 4.11 RMSE of the reconstructed AoP, ψ, as a function of incident polarization angle, left, and of incident intensity, S_0, right.

Figure 4.12 shows the RMS reconstruction error for the two calibration methods when run on the three single-wavelength datasets. Since the quantum efficiency of the sensor and polarization properties of the filters are wavelength dependent, the reconstruction errors also vary with wavelength. Since the extinction ratios of the filters are about 10 at 450 nm and increase to 30 at 550 nm and 38 at 650 nm, the errors for the blue dataset are highest—approximately 6% S_0

RMSE for intensities above 10%, while red and green light had errors close to 4% in the same range. Similar results were obtained for the RMSE of the DoLP and AoP.

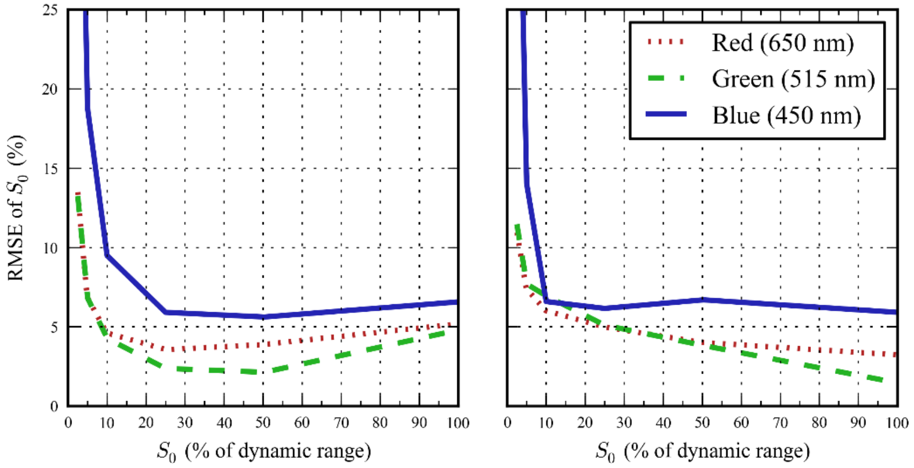

Figure 4.12 RMSE of the reconstructed intensity, S_0, as a function of the incident intensity for three different wavelengths. The left panel shows single-pixel calibrated reconstructions, the right panel uses the super-pixel calibration. Similar results were obtained for the RMSE of the DoLP and AoP.

4.2.4 Calibration of real-life images

Real-life images obtained from a DoFP polarimeter while driving on a rainy day are presented in Figure 4.13. The first row of images is uncalibrated. The intensity image suffers from vignetting at the right edge, the DoLP has a strong diagonal grain pattern, and the AoP deviates from the expected values—the road should be horizontally polarized but is closer to -30°, and the sky should have a gradient but is a constant 100°. The FPN in the DoLP and AoP images obscures most of the detail in the trees in the background of the scene.

The second row of images shows the results of applying the single-pixel calibration method. The vignetting of the intensity image is corrected, though there is a slightly brighter vertical band ¼ from the right edge of the image indicating that the vignetting has been overcorrected. Most of the FPN has been cleared from the DoLP and AoP images, revealing details in the road, vehicle, trees, and sky. However, the AoP of the roadbed approaches 15° towards the right side of the image, which is incorrect.

Finally, the third row of images shows the results of super-pixel calibration method. The bright band in the intensity image is reduced, slightly more detail is visible in the DoLP image, and the AoP of the roadbed is 0° across the image.

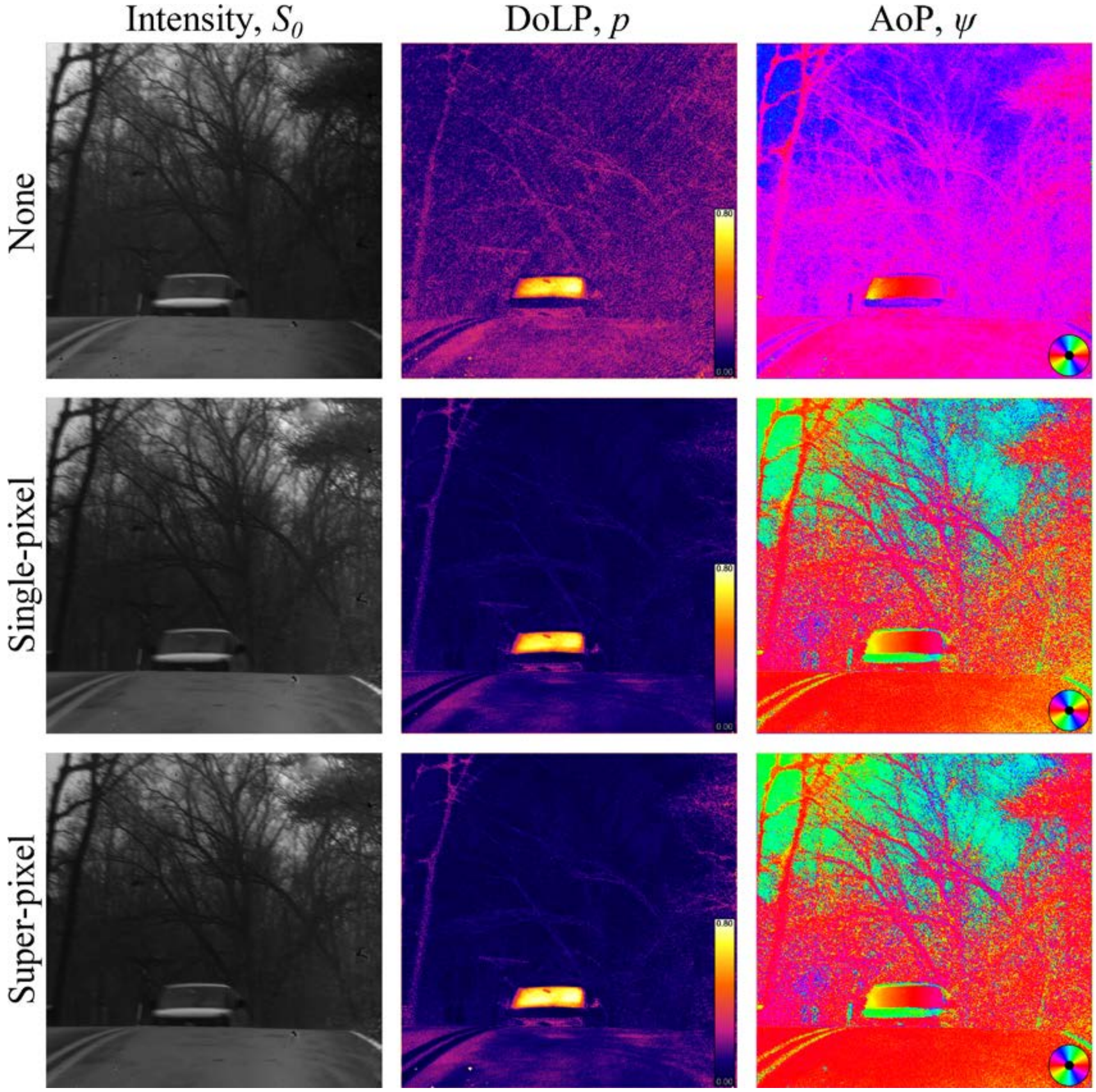

Figure 4.13 Real-life images obtained from a DoFP polarimeter. Each row shows the intensity image, S_0, the DoLP image, p, and the AoP image, ψ. The DoLP and AoP are presented in false color, scales are included in the bottom right of each panel. The intensity images have been contrast stretched. The top row shows uncalibrated images, the second row images have been calibrated with the single-pixel method, and the bottom row with the super-pixel method.

4.2.5 Summary

I have presented two calibration methods for division-of-focal-plane polarimeters. Typical division-of-focal plane polarimeters for the visible spectrum employ nanowire polarization filters. Flaws and mismatches in the dimensions of the nanowires lead to variations in the polarization properties of the filters at the macro scale, and I presented two calibration methods to mitigate these effects. Both methods were derived from the same linear model of the polarization pixels, but one treats each pixel independently and the other treats super-pixel groups together. I showed that the super-pixel approach is mathematically more powerful than the single-pixel approach and can correct for not only the typical variations in photodetector gain and offset, but also for variations in filter orientation and diattenuation. The single-pixel approach can only correct the variations in gain and offset.

The measurements of our visible-spectrum DoFP polarimeter show that a majority of the non-uniformity between pixels is in their filter transmission ratios, but a significant amount of variation occurs in filter orientation and diattenuation—parameters that the single-pixel calibration method cannot correct. Calibrating each pixel independently reduces DoLP reconstruction errors from 12% to 10% for moderate illumination levels. Calibrating each super-pixel as unit reduces the RMSE to approximately 1%. Similar reductions in error occur for intensity and AoP image reconstruction. These figures indicate that the super-pixel calibration method is worth the extra computational effort, but there are still un-addressed sources of error, including the sensor’s non-linear response, temporal noise, and non-uniformities in the flat-field that the calibration apparatus produces.

Finally, I showed that through the calibration parameters were measured using a broad-spectrum tungsten-halogen lamp with only an IR blocking filter in place, they performed well across the visible spectral range of the polarimeter. It is also worth noting that the optical properties of the polarimeter are stable enough that the same calibration parameters have been used with no measurable difference for about two years during the development of this work.

Chapter 5: Underwater Polarization Video Camera

5.1 Hardware Design

The underwater polarization video camera system was designed around the DoFP CCD polarization image sensor. The sensor was mounted in an Imperx Bobcat GEV camera body—this camera body is meant for industrial and research applications and provides flexible but precise control of the CCD's operation, including the configuration of the read-out amplifiers, analog-to-digital conversion, frame-rate, and integration times. The body also provides several high-level functions such as applying look-up tables to linearize the pixel response, flat fielding, setting various triggering modes, and automatic gain and exposure control. The body is controlled and serves live video via IP over a gigabit Ethernet link, which makes it easy to work with. Although the communication protocol is proprietary, there are software libraries available for Windows and Linux operating systems.

The system was enclosed in a Light and Motion Bluefin VX2000 underwater housing. This housing is rated to depths up to 100 m and has a 3" front lens port with glass optics. Glass optics are important for polarization applications because acrylics are often birefringent and have polarization effects that change significantly with strain—a serious issue for an instrument that will be subjected to high pressures. The housing also includes integrated control buttons in the handles that emit IR remote control signals into the housing when pressed.

For imaging optics, I primarily used the Canon EF-S 18-55 mm lens. The lens mount was modified to hold a custom circuit board with spring-loaded "pogo pins" to contact the pads on the edge of the proximal end of the lens. These pins are used to detect the presence of the lens, provide power to the lens's motors, and connect to the lens's serial control interface. The serial interface uses a slight variation on the SPI protocol and allows control of the focus and aperture, and feedback on the current focal length of the lens.

The orientation of the instrument was measured using a PNI Sensor Corporation TCM MB electronic compass module. This module contains a 3-axis magnetometer and a 3-axis accelerometer and provides magnetic heading, roll, and pitch information at 30 Hz over a serial interface. The module includes a calibration procedure for removing both hard-iron and soft-iron effects and claims accuracy better than 0.5° RMS when calibrated.

An ADL QM67PC-2715QE single-board computer with an Intel Core i7 quad-core processor and a 512 GB solid-state drive was used for control and data logging. This computer was compact enough to fit within an underwater housing, but also provided enough data bandwidth and computational power to both record the uncompressed video stream to disk (~ 20 MB/s) and present a user interface with live polarization video to the operator on an external SmallHD HDMI monitor.

A PJRC Teensy 3.2 ARM microcontroller board was connected to the PC via USB and used to translate the housing buttons’ IR signals into the USB keyboard protocol and translate the Canon lens SPI protocol into a USB serial device. It was also patched into the PC’s power button circuit and used to “press” the button, but only to turn the machine on. Powering down the machine was always left to software control so that all data could be written to disk cleanly first.

Power to the system was provided by an ADL PS35-150-12 switching power supply. This power supply has a wide DC input voltage range, from 14 V to 36 V, making it suitable for use with batteries, and also complies with ATX signals for computer control. For typical use, I used Tenergy 14.8V 5.5Ah lithium-ion polymer battery packs which allowed approximately 2 hours of continuous run-time—enough for most SCUBA dives.

The housing was modified to hold the camera on a removable sled for easy access. Idler wheels were added to the front of the housing to keep the lens centered on the front port, and one of the through-hull rotary shafts was modified to mesh with the lens's zoom ring. The computer, power supply, and compass module were semi-permanently mounted on an aluminum plate above the camera. The plate fits flush against the walls of the housing to dissipate heat into the surrounding water while the camera is in operation. Connectors for the battery, the camera, and the lens, along with two USB ports were panel-mounted at the rear of the camera in an easily accessible panel. Only brass and aluminum were used for the mounting hardware to minimize magnetic effects. The monitor was attached externally in a Nauticam NA-DP4 housing and connected to the computer via a through-hull HDMI connector. Figure 5.1 shows a schematic diagram of the system's hardware, while Figures 5.2 through 5.6 show photographs of the system's components.

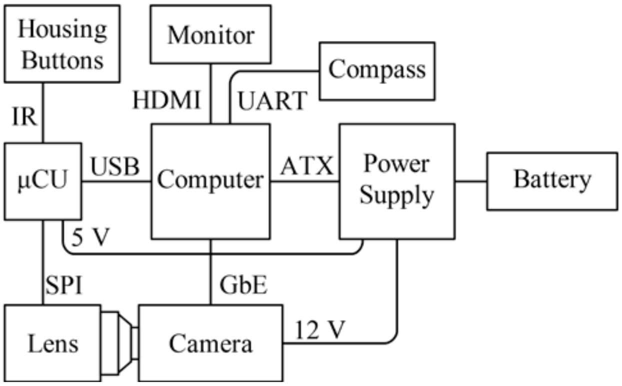

Figure 5.1 Schematic diagram of the system showing major components and connections.

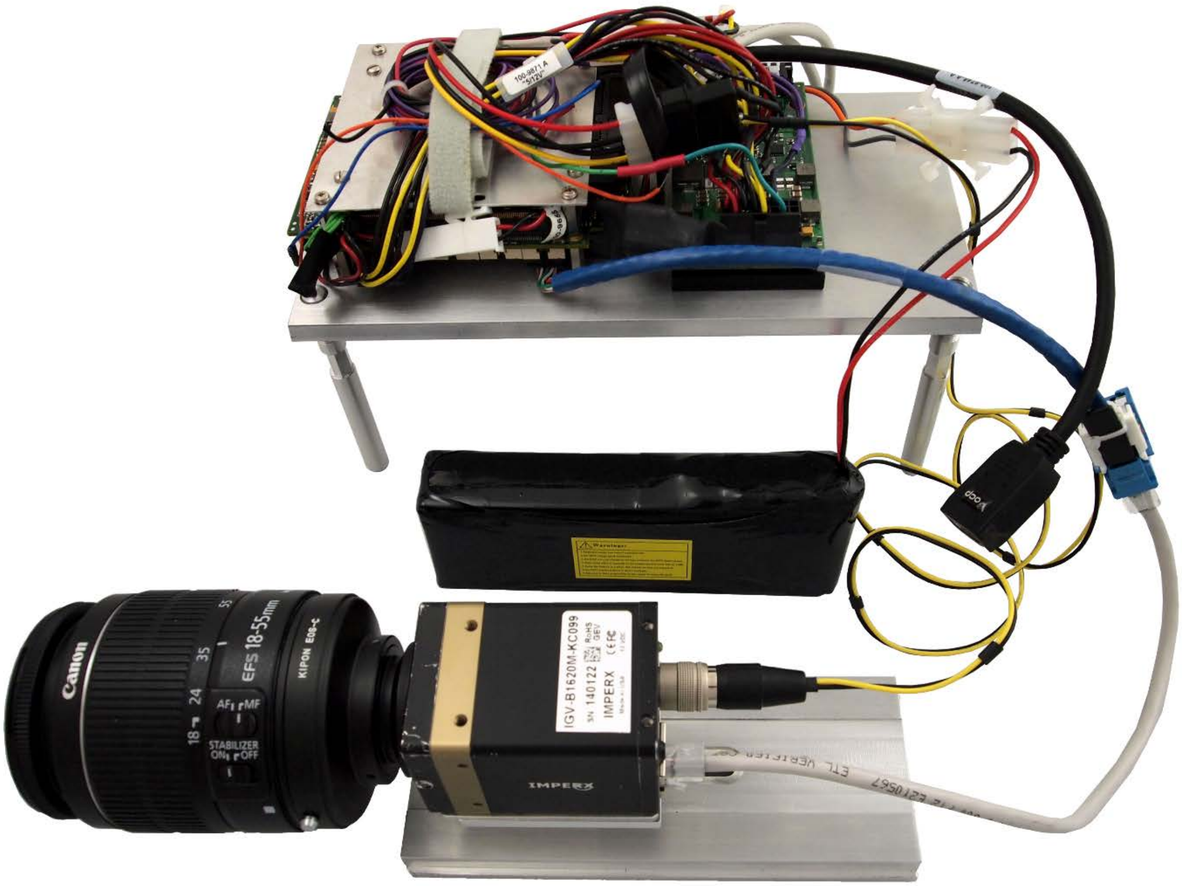

Figure 5.2 From top to bottom: The computer and power supply are mounted on an aluminum plate with legs to hold it above the camera. A rechargeable lithium-ion battery provides power. The camera is mounted on an aluminum sled that fits beneath the computer. This version of the system does not have a compassmodule or a panel for mounting connectors.

Figure 5.3 The customized Canon EF-S to c-mount lens adapter with spring-loaded pins for electronically controlling the lens.

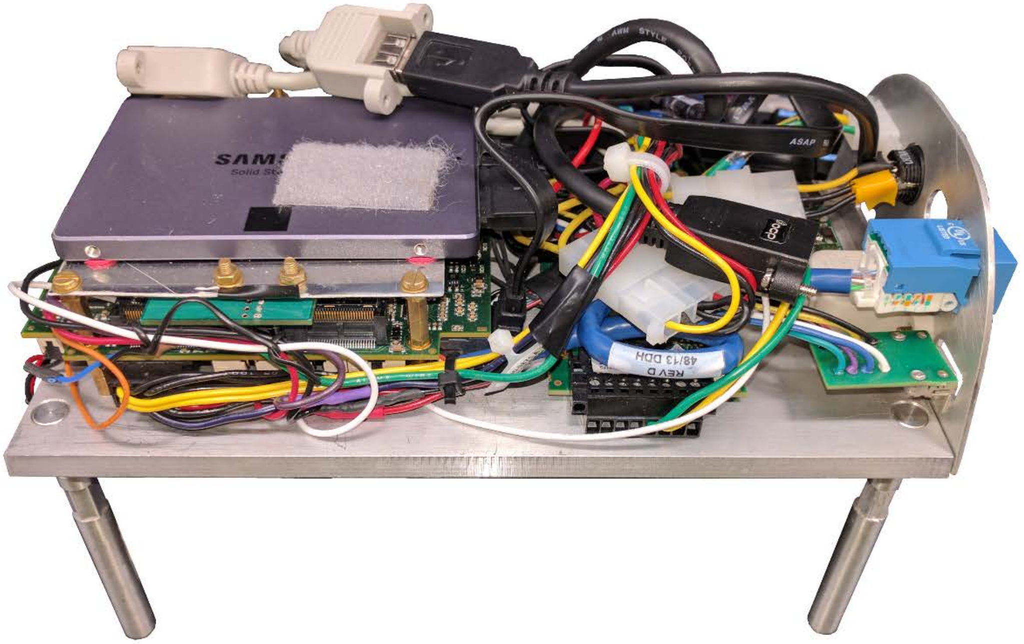

Figure 5.4 The latest revision of the computer, including the compass module and connector panel. All of the mounting hardware is brass to minimize magnetic effects.

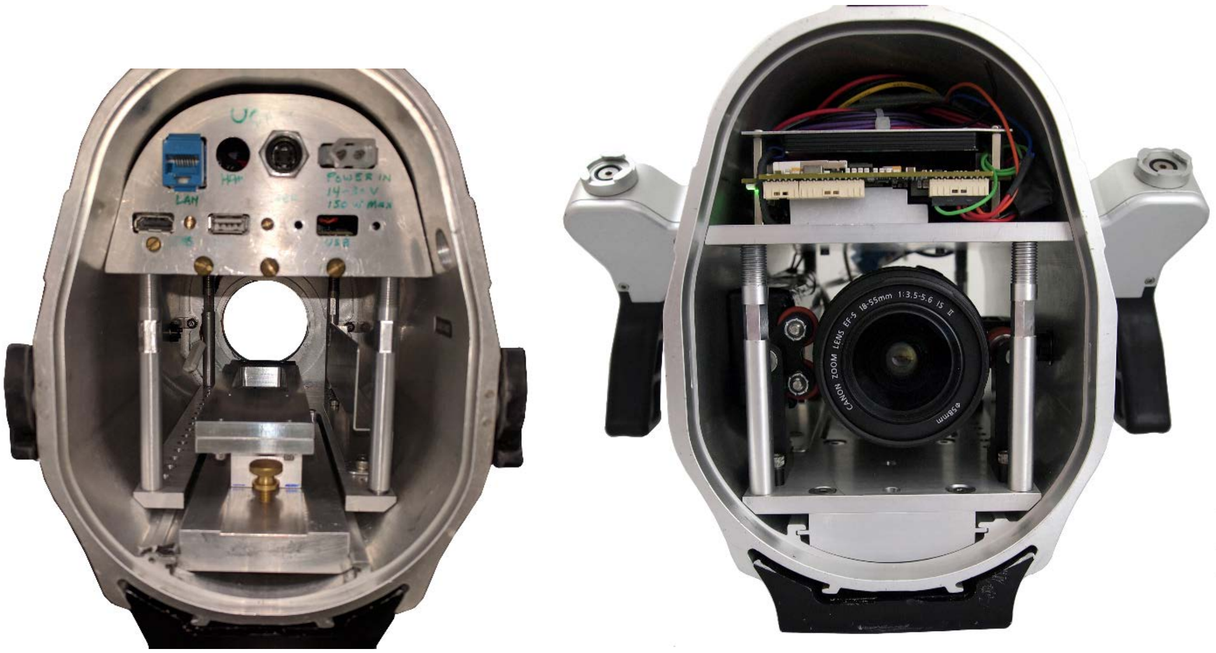

Figure 5.5 Left: The rear of the camera housing, showing the connector panel. The camera sled is installed below without a camera. The bracket inside the housing on the right holds the battery. Right: The front of the housing, showing the computer mounted above the camera. Idler wheels hold the lens steady.

Figure 5.6 The camera, sealed and prepared for a dive. The monitor is mounted on the top of the housing. A small color video camera is mounted on an arm to the right of the housing, and polarization filters are on the left. Extra ballast is taped to the rear of the housing to balance the weight of the monitor.

5.2 Software Design

The system software consists of two major components: the live control software that runs on the underwater camera, and a suite of post-processing software for analyzing recorded data. The control software runs in real-time, records all of the sensor data at the framerate of the image sensor, displays live polarization video and other sensor readings to the operator, and allows the operator to control the device in several modes. The post-processing application provides a graphical user interface for reading recorded data files and allows fine control over how the polarization images are processed and displayed. It displays all of the sensor data recorded with each frame of video and provides a feature for querying the average polarization state at points on the image. It can save processed still images or render the data to standard video file formats.

5.2.1 Live Control Software

The embedded computer in the underwater housing runs on the Linux operating system, chosen for its small footprint and flexibility, especially in scripted control of network services and power management. The specific Linux distribution is CentOS 7, which is supported by the camera manufacturer's software libraries. For ease of management, the system was configured to allow local SSH connections and a SMB file share was configured to expose the software and recorded data directories. At boot, the system runs a script that first uses the `tee` utility to redirect all console messages to a log file for debugging purposes. The script configures the machine's network interface, briefly attempting to acquire network setting via DHCP before defaulting to the link-local addressing used by the camera. Then the script parses several configuration files and based on their content launches a C++ program for controlling the machine in either normal or time-lapse mode.

In both modes, the C++ program operates in two phases: first it connects to and configures all of the sensors and peripherals, then it enters a real-time loop acquiring, recording, and displaying information from the sensors and camera. In normal mode, the operator has live control of the camera's exposure, lens focus and aperture, and whether the machine is recording data. In time-lapse mode, however, the program enters a state machine that records a certain number of frames at several exposure brackets, then uses the `rtcwake` utility to put the machine into a low power state until the time lapse interval has passed.

The C++ program is designed to operate robustly while in the field. Except for the image sensor, if the software fails to connect to a peripheral or sensor, the software continues and simply ignores the missing device. The software uses the HDF5 file format, a flexible and widely used scientific data format [62]. While recording, the software starts a new file every 2 minutes so that minimal data is lost if a hard crash occurs. The user interface shows the relevant machine state in large, high-contrast block letters, uses cyan to highlight errors and over-saturated pixels because red does not contrast well underwater, and displays a large X over the screen if the software is not recording data.

The live control software has two performance constraints: it must be able to consume and record data from all of the sensors at the framerate of the image sensor and provide responsive control to the operator. For this reason, the OpenMP parallelization strategy, described in §3.1, was chosen. To meet the performance requirements on the underwater camera's hardware, the algorithm was further parallelized using the SSE vector instructions for floating point math, and the calibration and interpolation steps of the image processing algorithm were skipped. While skipping the interpolation step does introduce polarization aliasing artefacts, such images still display enough useful information for the camera operator to make informed decisions about the camera settings. Because the system always records the raw sensor output, the artefacts are not present in any final analyses.

5.2.2 Post-Processing Software

The post-processing software is a Windows application that uses the Qt library to provide a user interface. The software reads the recorded data files produced by the underwater camera system and presents reconstructed polarization images along with all of the sensor data for each frame. The software allows control of the polarimetric calibration, interpolation algorithm, masking of over- and under-exposed pixels, and false-color mapping. Users can query the polarization state of the image at points in the image, and also compute the average polarization state in circular regions. Overlays of the instrument heading, date and timestamp, and polarization state can be added to the rendered data as well. The software can save rendered still frames to common image formats, and uses the ffmpeg library to encode the rendered data to common video formats.

Chapter 6: Underwater Navigation

This chapter contains material from “Polarization Vision Enables Underwater GPS-Free Navigation”, submitted to Nature for review.

Polarized light features prominently in shallow underwater environments. Light from the sun and sky is selectively refracted at the water’s surface and scatters within the water, creating complex patterns of polarization states in the underwater light field [22]. These polarization patterns have been observed as deep as 200 m [30] and are dependent on many environmental factors [63], but primarily the position of the sun in the sky [23]. Here we show that it is possible to infer the sun’s position (heading and elevation angle) without direct observation using the underwater polarization patterns. Our inference is based on comparing measurements of in-water polarization states from a bio-inspired imaging polarimeter [32] to the output of a single-scattering optical model augmented with residuals learned from experimental data. We inferred the sun’s apparent heading and elevation with root-mean-square (RMS) errors of 6° and 2.9°, respectively, and estimated global position with an RMS error of 442.5 km when the sun was at least 40° above the horizon. Sensitivity measurements of our instrument show that it can detect the difference in polarization patterns between two sites 46.9 km apart with 99% confidence. Our results serve as a proof of concept for a new mode of underwater navigation based on passive observations of in-water polarization states. This technique could be used by underwater vehicles for long-distance navigation and suggests additional mechanisms by which marine animals with polarization sensitive vision might perform both local and long-distance navigation.

Navigation using photoreceptor arrays specifically sensitive to the pattern of the polarization of light in the sky is well documented in terrestrial animals, especially among arthropods such as ants, bees, crickets, dung beetles, and spiders [18, 19, 64]. Honey bees journeying to and from hives rely on the predictable pattern of polarized light relative to the sun's position [17], for example, and longer range migration in birds may use polarization as a cue [20, 21]. The polarization patterns of underwater light have similar structure to those in the sky, and follow predictable trends based on the position of the sun [23]. The intensity and partial polarization of underwater light are highly sensitive to many environmental factors in addition to the sun's position, including atmospheric conditions, water quality, and depth [65]. However, the patterns in the polarization angle (also known as the e-vector angle) are less sensitive to perturbations and thus serve as a stable proxy for the sun's position [22, 23]. Many marine animals are known to have polarization-sensitive vision [25], which has a variety of hypothesized uses from improving visual contrast for predator and prey detection [66] to covert communication [28]. Several works have focused on how salmonids could use the polarization patterns of the sky for orientation [29], though it has also been hypothesized that the in-water polarization patterns may be used for animal navigation as well [31, 67]. Here we report a method for inferring both the sun's heading and elevation from measurements of in-water polarization angles. Our results show that in addition to being suitable for a compass, the polarization patterns can also be used for determining global position.

Two optical phenomena, scattering and refraction, are mostly responsible for the underwater polarization patterns. As shown in Figure 6.1, light from the sun and sky (itself a product of scattered sunlight) enters the water by refracting through the surface. The refraction bends the light such that the image of the celestial hemisphere is compressed into an approximately 97° cone known as Snel's window. The transmitted light waves are preferentially polarized in the plane of the incident and refracted rays. The bulk of the light outside of Snel's window—what we call in-water light—is refracted sunlight that has scattered from the water itself [68], but some of it is internally reflected light from the underside of the water's surface or reflected light from the sea floor or arbitrary objects. Scattering events partially polarize the light perpendicular to the plane that the incident and scattered rays lie in [69], which produces a general trend of polarization perpendicular to the refracted ray. Figure 6.2 shows the polarization pattern produced by this combination of refraction and scattering. In certain situations, particularly when the sun is low in the sky, it is possible for the polarization effect of the refraction to cancel or even dominate that of the scattering. This causes "neutral points" in the polarization state of the light field facing the sun and away from it, where the partial polarization drops to zero and the polarization angle abruptly transitions from horizontal to vertical [22]. At increasing depths or decreasing water clarity, multiply-scattered light becomes more prevalent—this increases the homogeneity of the observed polarization states, resulting in less partial polarization and polarization angles that are closer to horizontal [22, 65]. However, sun-dependent patterns in the polarization angle have been observed as deep as 200 m [30].

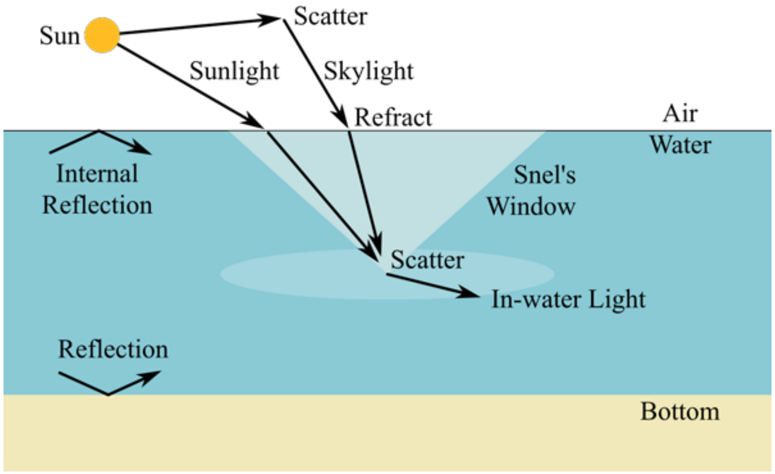

Figure 6.1 Light in the underwater environment.

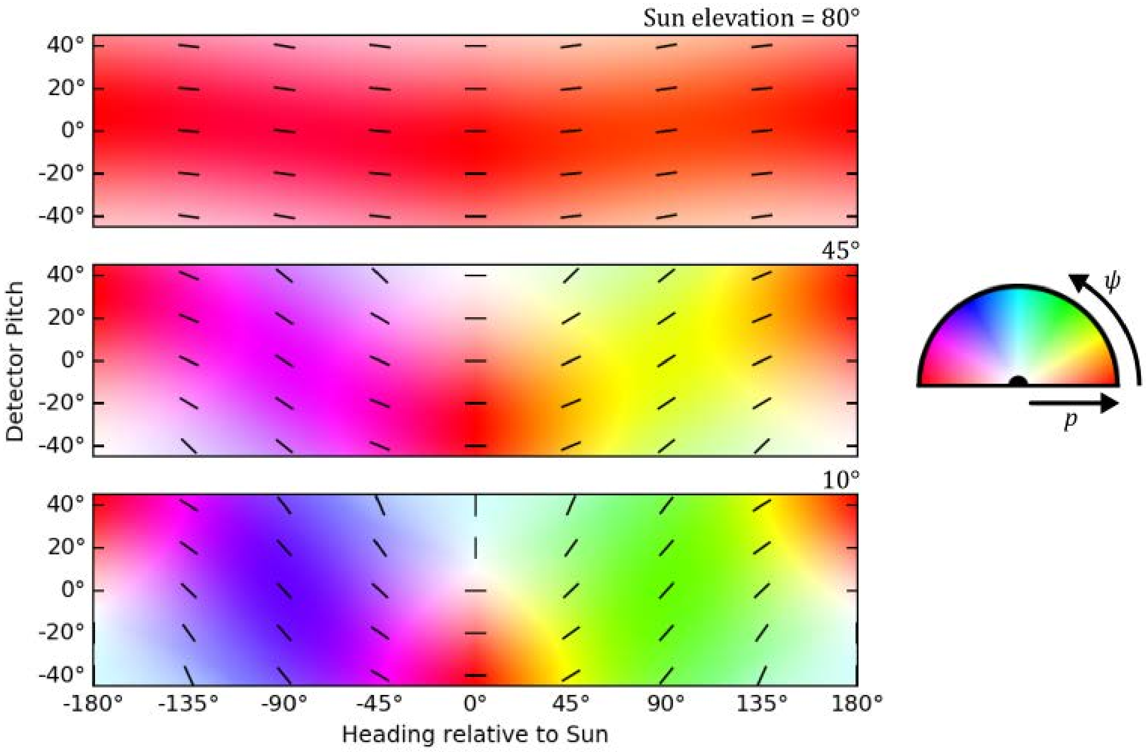

Figure 6.2 Underwater polarization patterns outside of Snel's window caused by the refraction and scattering of sunlight. Polarization state is shown in false color, as indicated by the scale on the right. For clarity, a grid of lines oriented at the polarization angles has been drawn over the plots as well. Note the neutral points, where the DoP approaches 0 and the AoP transitions from 0° to 90°, that occur at low sun elevation.

Figure 6.3 shows the polarization states that an animal with polarization-sensitive binocular vision might observe about the horizontal plane. For illustrative purposes, we restrict the animal's vision to detect polarization angles only in small regions 40° to the left and right of the creature's heading. Figure 6.4 shows that a unique pair of polarization angles is observed by the animal for each relative heading and sun elevation. This implies that over short time-scales the animal can maintain its heading simply by keeping these two observed polarization angles constant. Over longer distances or durations the animal will need to compensate for the movement of the sun through the sky. Additionally, the one-to-one mapping implies that it is possible to infer the sun's relative position from such observations. Thus, with access to a compass, an accurate timepiece, and an almanac, our animal can determine its latitude and longitude as well.

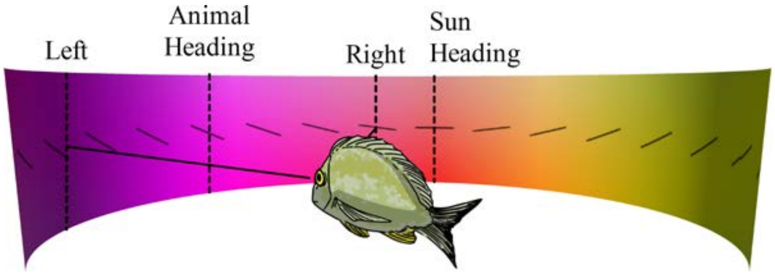

Figure 6.3 The polarization angles a hypothetical animal would observe about the horizontal plane.

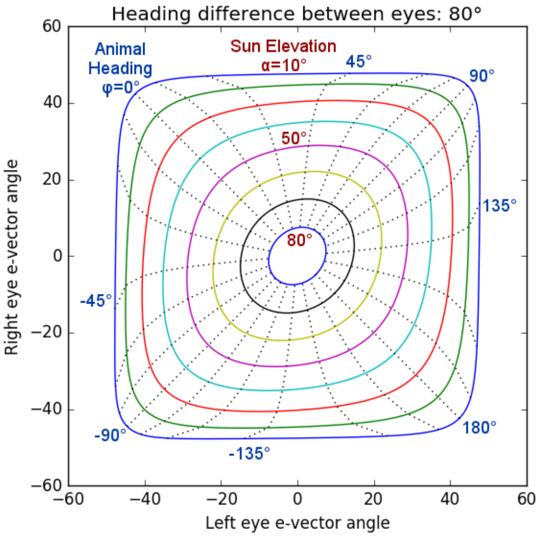

Figure 6.4 The polarization angles observed by the animal in Figure 6.3, plotted as the animal heading changes relative to the sun (radial dotted lines), at sun elevations from 10° above the horizon to 80° above the horizon.

We collected data for inferring the sun's position from in-water polarization angles using a bio-inspired, visible-spectrum, imaging polarimeter [32]. The sensor mimics the polarization-sensitive vision system of certain species of mantis shrimp by integrating polarization optics with the individual pixels of a camera. More specifically, polarization filters comprised of parallel aluminum nanowires (140 nm thick by 70 nm wide) were aligned and deposited onto each pixel of a low-noise, two megapixel CCD image sensor. The filters are variously oriented at 0°, 45°, 90°, and 135° in a repeating 2-by-2 pattern across the focal plane—this enables the polarimeter to capture intensity, partial polarization, and polarization angle images. This bio-inspired polarization camera was paired with an electronic compass and tilt sensor within an underwater housing to measure the in-water polarization angles versus heading at a variety of sites, depths, and times of day (see §6.1).

To infer the sun's position, we used a general-purpose optimization algorithm to match the measured polarization angle patterns against the predictions of a basic single-scattering model of underwater light, described in §6.2. Figure 6.5 shows several example measurements compared to the model output and Figure 6.6 shows the average model residuals of all experiments. The model agrees with the measurements when the sun is at least 40° above the horizon. When considering just these experiments, we estimate the sun's position with RMS errors of 8.57° in heading and 5.82° in elevation. These in turn lead to a global positioning RMS error of 817 km.

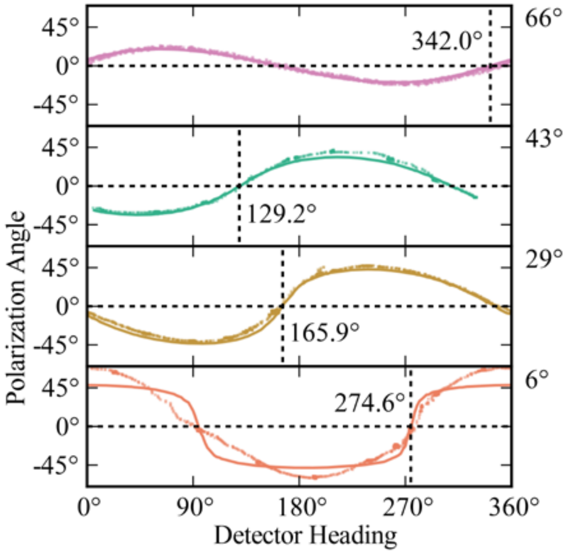

Figure 6.5 Example measurements of the in-water polariztion angle (dots) compared to the single scattering model (lines). Vertical dotted lines indicate the sun's heading. The sun's elevation is indicated by the angles on the right.

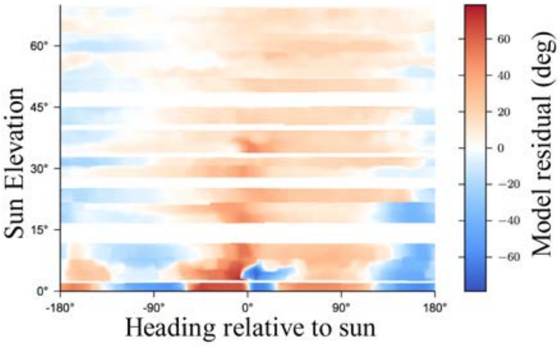

Figure 6.6 The average model residuals at each heading and sun elevation is computed using a kernel density estimator. The magnitude of the residuals is shown in false color, according to the scale on the right. The horizontal white bands occur where no data was measured.

The smoothly varying nature of the residuals indicates that there are additional dependencies between the in-water polarization angle and the sun's position that the single-scattering model does not capture. We incorporate these dependencies into our system by using a *k*-nearest-neighbors (*k*NN) regression [70] to estimate the residuals of the model evaluated at the sun's true position, as a function of the naïvely estimated sun position. By subtracting the estimated residuals from our measurements during a second phase of inference, we can remove a significant amount of error: the RMS errors of the sun's heading and elevation reduced by 30% and 50% to 6.02° and 2.92°, respectively, and the global position estimate RMS error improved by 46% to 442 km. Figure 6.7 shows the distribution of global position estimates, and the improvements introduced by the *k*NN regression, from experiments performed at Lizard Island Research Station in north-eastern Australia. Table 6.1 lists the error statistics from these measurements.

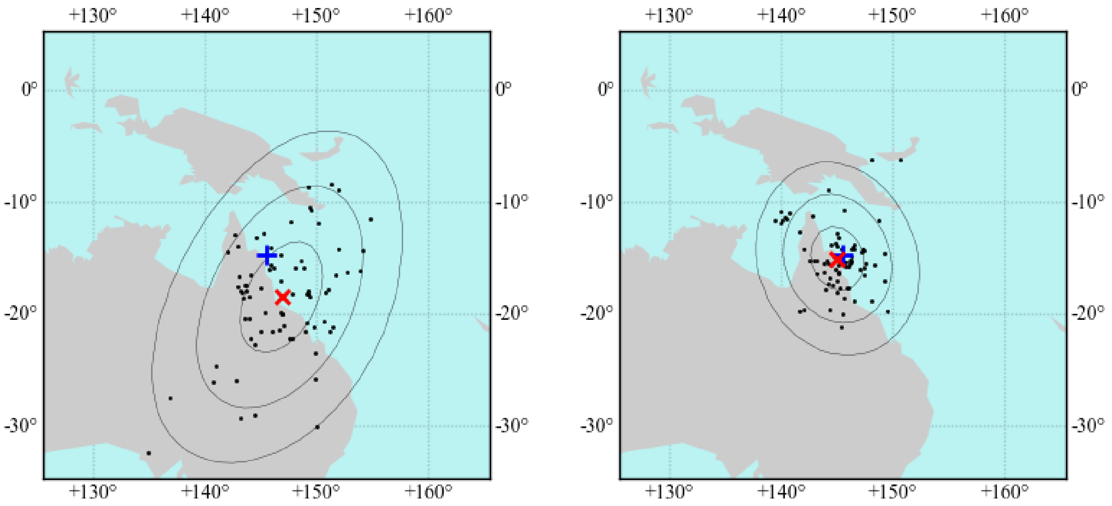

Figure 6.7 Global position estimates from data collected at Lizard Island Research Station in northern Australia when the sun was at least 40° above the horizon. The blue plus shows the location of the collection site, black dots show the position estimates, and the red ex shows the centroid of the position estimates. The concentric rings show 1, 2, and 3 standard deviations around the data. The left panel shows the position estimates using just the single-scattering model. The right panel shows the position estimates with the *k*NN residual estimates.

	Sun Heading RMSE		Sun Elevation RMSE		Position RMSE	
Site	Naïve	kNN	Naïve	kNN	Naïve	kNN
Electric Beach	8.78°	**3.46°**	5.37°	**5.07°**	928 km	665 km
Lizard Island	8.54°	**6.23°**	5.87°	**2.60°**	805 km	**412 km**
All	8.57°	**6.02°**	5.82°	**2.92°**	817 km	**433 km**

Table 6.1 Sun position and global position RMS error statistics for experimental data taken when the sun was at least 40° above the horizon. Bolded values are significantly ($p < 0.05$) better than their counterparts.

The model performance as the sun approaches the horizon suffers, likely because it does not include skylight, which contributes an increasingly large fraction of the light hitting the ocean's surface as the sun drops below 40° above the horizon [71]. When we include this low-elevation data, our naïve inference method achieves RMS errors of 9.22°, 8.07°, and 2,915 km in sun heading, sun elevation, and global position, respectively. Incorporating the *k*NN residuals model reduces these by 41%, 23%, and 32% to 5.46°, 6.23°, and 1,970 km, respectively. Curiously, the accuracy of the *k*NN heading estimates improves when the low-elevation data is included, possibly because the polarization angle patterns develop a very strong gradient facing the sun's heading. However, the lack of improvement in the sun elevation estimate renders this improvement moot for the purposes of global positioning. Figure 6.8 and Figure 6.9 show the global position estimates from all of the experiments. Table 6.2 lists the RMS error statistics for all of the experiments, including low sun elevations.

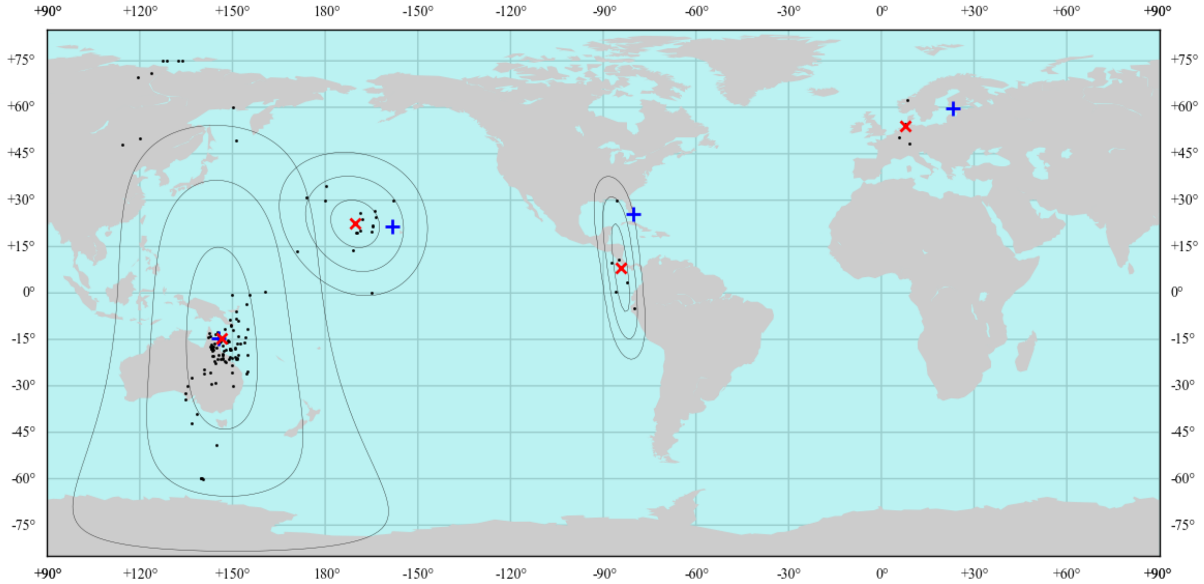

Figure 6.8 Global position estimates from all experiments, using only the single-scattering model. The blue plusses show the locations of the collection sites, black dots show position estimates, and red exes indicate the centroid of the position estimates from each site. The concentric rings show 1, 2, and 3 standard deviations around each centroid, estimated with the Kent distribution. There was not enough data collected at Tvärminne, Finland to fit the Kent distribution parameters.

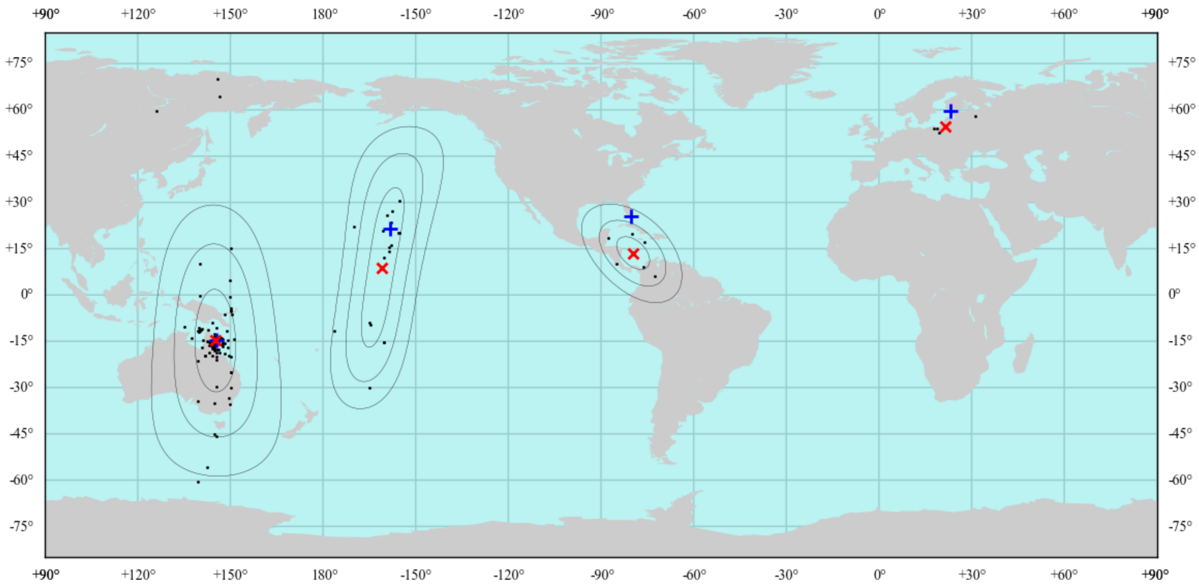

Figure 6.9 Global position estimates from all experiments, using the *k*NN residual estimation. Displayed as in Figure 6.8.

	Sun Heading RMSE		Sun Elevation RMSE		Position RMSE	
Site	Naïve	kNN	Naïve	kNN	Naïve	kNN
Tvärminne	13.03°	**4.82°**	5.93°	5.13°	1300 km	**704 km**
Electric Beach	8.82°	**4.70°**	11.40°	10.80°	1720 km	2511 km
Miami	14.28°	**6.99°**	4.36°	7.36°	2345 km	1573 km
Lizard Island	8.73°	**5.50°**	7.60°	**5.02°**	3143 km	**1918 km**
All	9.22°	**5.46°**	8.07°	**6.23°**	2915 km	**1971 km**

Table 6.2 Sun position and global position RMS error statistics for all experimental data. Bolded vales are significantly ($p < 0.05$) better than their counterparts.

While these errors may seem impractically large—following a heading 6° off course would result in a 105 m error after traveling 1 km—note that the RMS statistic includes a measure of the variance. When navigating with a noisy compass one would use the average reading over time, not pick a single heading and follow it blindly. In the high-sun case, the mean heading error was just 0.38° (6.6 m over 1 km), which is commensurate with the polarization-compass abilities of the desert ant [72]. In a similar fashion, it is more realistic to consider the average of our global position estimates rather than treat them independently. As shown in Figure 6.7, the centroid of position estimates performed in northern Australia is only 61 km from the true measurement location. Table 6.3 lists these errors for all of the experimental sites. While achieving this resolution required averaging 76 estimates, an animal or underwater vehicle would almost certainly be performing path integration or using a Kalman filter to integrate and smooth the noisy measurements over the course of the day [14, 73]. In that case, including knowledge of the sun's trajectory through the sky would further constrain the inference problem and reduce all of the errors as well.

	Mean Heading Error		Position Centroid Error	
Site	Naïve	kNN	Naïve	kNN
Electric Beach (> 40°)	-8.76°	**-2.42°**	79 km	574 km
Lizard Island (> 40°)	-3.96°	**0.68°**	416 km	36 km
All (> 40°)	-4.42°	**0.38°**	-	-
Tvärminne	-12.89°	**-1.19°**	664 km	581 km
Electric Beach	-8.07°	**2.58°**	89 km	1382 km
Miami	-13.66°	**-5.62°**	1943 km	1349 km
Lizard Island	-5.17°	**0.52°**	118 km	13 km
All	-6.18°	**0.47°**	-	-

Table 6.3 Mean heading error and position estimate centroid error, by site. The first three rows list errors for experiments performed when the sun was at least 40° above the horizon. Bolded values are significantly ($p < 0.05$) better than their counterparts. No statistical tests were performed on the position centroid errors.

In addition to testing the inference algorithm on experimental data, we also performed a sensitivity study of our instruments (see §6.4). The instrument was capable of detecting changes to the in-water polarization angle pattern caused by a 0.31° movement of the sun with 99% confidence, which corresponds to a movement of 33 km along the latitude where the sensitivity measurements were performed. This implies that a majority of the positioning error in our system is due to model errors rather than the sensor performance. To achieve this level of accuracy in the inference problem, there are several clear targets for improvement. First and foremost, the poor performance of the single-scattering model at low sun elevations must be addressed—without a reasonable initial estimate of the sun's position, no machine learning algorithm would be able to reduce the model errors. The second target is to infer the sun's path through the sky over time rather than a singular position—the constraint that the sun follows a continuous arc through the sky would help reject much noise from the system. Finally, additional training data under more varied conditions would boost the performance of the residual estimation step.

Our results show that the in-water polarization angles can reasonably serve as a solar compass for animals with polarization-sensitive vision and can also be used to determine global location with moderate accuracy. This study also provides insight into an additional navigation method for animals with polarization sensitive vision.

6.1 Sun Position Inference Data Collection

Polarization data for sun position inference was collected at Lizard Island Research Station, Australia; Hawaiian Electric Beach Park, Hawai'i; Miami, Florida; and Tvärminne Zoological Station, Finland. The measurements were performed by SCUBA divers at depths from 2 to 20 m, at times of day varying from sunrise to sunset. Dive site locations were recorded at the surface with a Garmin Oregon 700 GPS receiver. The instrument was mounted on a tripod such that it rotated freely about the vertical axis, and pitched such that neither the water surface nor the sea floor was visible in the center of the field of view, as shown in Figure 6.10. The operating diver then measured the instrument depth with their dive computer. For each recording, the instrument was rotated once around the vertical axis, pausing approximated every 45° to allow the compass and tilt sensor to settle. Recordings were typically less than 2 minutes in duration, and anywhere from 2 to 10 were collected per dive depending on the circumstances.

Figure 6.10 The underwater polarization camera prepared for a sun position inference experiment.

To process these recordings, we polarimetrically calibrated each video frame as described in Chapter 4 and cropped them to a 100×100-pixel region at the center of the field-of-view. We computed the average Stokes vector over the region, and extracted the polarization angle from it. Frames were rejected if they contained the sea floor, water surface, objects, bubbles, or animals in the region of interest, or if the sun was visibly shaded by clouds or nearby boats. The compass measurements were smoothed by applying a low-pass sinc filter with a -3 dB frequency of 1.35 Hz.

6.2 Single Scattering Model

The single-scattering model of underwater polarization states is based on the Mueller-Stokes formalism of representing polarized light. A diagram of the model is shown in Figure 6.11. Each ray of polarized light is represented by a 3-tuple $(\boldsymbol{S}, \boldsymbol{k}, \boldsymbol{x})$ where $\boldsymbol{S} \in \mathbb{R}^4$ (W/m^2) is the Stokes vector of the light, $\boldsymbol{k} \in \mathbb{R}^3$ (rad/m) is the wave vector, which points in the direction of the light's phase velocity and has magnitude $\|\boldsymbol{k}\| = 2\pi/\lambda$, and $\boldsymbol{x} \in \mathbb{R}^3$ is a unit-vector perpendicular to $\boldsymbol{k}$ that indicates the "horizontal" orientation for interpreting $\boldsymbol{S}$. Optical events are modeled by left-multiplying the Stokes vector by a Mueller matrix $\mathbf{M} \in \mathbb{R}^{4\times4}$.

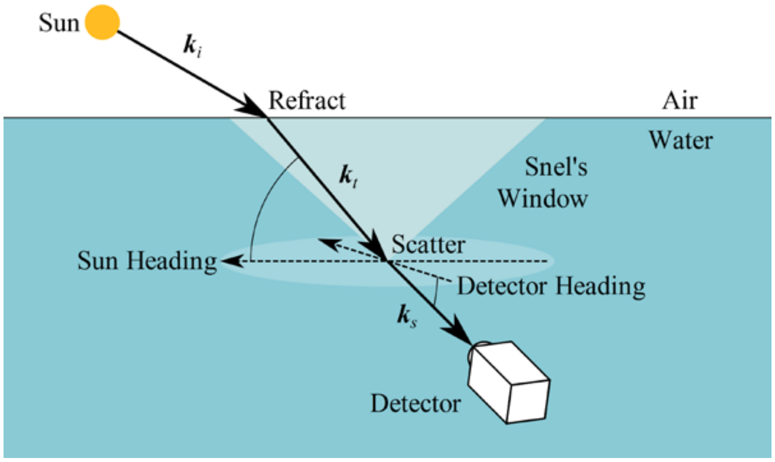

Figure 6.11 Diagram of the single-scattering model.

The first optical event of the model is the refraction of incident light from the sun or sky, $(\boldsymbol{S}_i, \boldsymbol{k}_i, \boldsymbol{x}_i)$ through the water's surface. The air-water interface is defined by the surface normal $\boldsymbol{n} \in \mathbb{R}^3$, which points from the water to the air, and the real indices of refraction of the air and water, η_i and η_t, respectively. The transmitted light $(\boldsymbol{S}_t, \boldsymbol{k}_t, \boldsymbol{x}_i)$ is computed per Snel's law and Fresnel's equations, with the $\boldsymbol{x}$-vectors lying in the water surface, as shown in Figure 6.12.

$$\boldsymbol{k}_t = \boldsymbol{k}_\parallel - \boldsymbol{n}\sqrt{(\eta_t/\eta_i)^2\|\boldsymbol{k}_i\|^2 - \|\boldsymbol{k}_\parallel\|^2}, \qquad \boldsymbol{k}_\parallel = \boldsymbol{k}_i - (\boldsymbol{k}_i \cdot \boldsymbol{n})\boldsymbol{n} \tag{6.1}$$

$$\boldsymbol{x}_t = \boldsymbol{x}_i = \frac{\boldsymbol{n}\times\boldsymbol{k}_i}{\|\boldsymbol{n}\times\boldsymbol{k}_i\|} \tag{6.2}$$

$$\boldsymbol{S}_t = \mathbf{M}_R \boldsymbol{S}_i \tag{6.3}$$

$$\mathbf{M}_R = \frac{1}{2}\begin{pmatrix} t_s^2 + t_p^2 & t_s^2 - t_p^2 & 0 & 0 \\ t_s^2 - t_p^2 & t_s^2 + t_p^2 & 0 & 0 \\ 0 & 0 & 2t_s t_p & 0 \\ 0 & 0 & 0 & 2t_s t_p \end{pmatrix} \tag{6.4}$$

$$ts = \frac{2\boldsymbol{k}_i \cdot \boldsymbol{n}}{(\boldsymbol{k}_i + \boldsymbol{k}_t) \cdot \boldsymbol{n}}, \qquad t_p = \frac{2\eta_i \eta_t \boldsymbol{k}_i \cdot \boldsymbol{n}}{(\eta_t^2 \boldsymbol{k}_i + \eta_i^2 \boldsymbol{k}_t) \cdot \boldsymbol{n}} \tag{6.5}$$

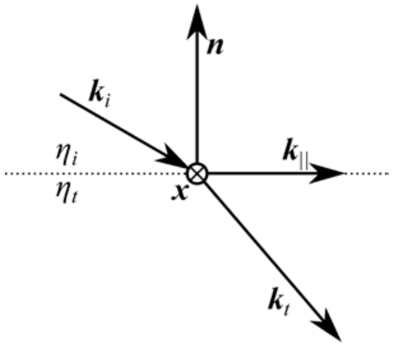

Figure 6.12 Refraction geometry.

The second optical event is the scattering of the transmitted light. The wavevector of the scattered light, $\boldsymbol{k}_s$, is the same magnitude as $\boldsymbol{k}_t$ but points to the detector. The typical coordinate system for representing scattering events, illustrated in Figure 6.13, has the $\boldsymbol{x}$-vectors of the incident and scattered light lying in the same plane as the wavevectors, thus $\boldsymbol{S}_t$ must be rotated by a coordinate transform matrix $\mathbf{M}_{R\to S}$, as described in Eq. 2.8, before being multiplied by the scattering matrix $\mathbf{M}_S$. We model the polarization effects of scattering using the Rayleigh approximation, but renormalized so the intensity follows $\tilde{\beta}_{FF}(\theta)$ (sr^{-1}), the Fournier-Fourand volume scattering phase function.

$$\|\boldsymbol{k}_s\| = \|\boldsymbol{k}_t\| \tag{6.6}$$

$$\boldsymbol{x}_s = \frac{\boldsymbol{y}_s \times \boldsymbol{k}_s}{\|\boldsymbol{y}_s \times \boldsymbol{k}_s\|}, \qquad \boldsymbol{x}_{t,s} = \frac{\boldsymbol{y}_s \times \boldsymbol{k}_t}{\|\boldsymbol{y}_s \times \boldsymbol{k}_t\|}, \qquad \boldsymbol{y}_s = \frac{\boldsymbol{k}_t \times \boldsymbol{k}_s}{\|\boldsymbol{k}_t \times \boldsymbol{k}_s\|} \tag{6.7}$$

$$\boldsymbol{S}_s = \mathbf{M}_S \mathbf{M}_{R\to S} \boldsymbol{S}_t \tag{6.8}$$

$$\mathbf{M}_S = \frac{\tilde{\beta}_{FF}(\theta)}{c_\theta^2 + 1} \begin{pmatrix} c_\theta^2 + 1 & c_\theta^2 - 1 & 0 & 0 \\ c_\theta^2 - 1 & c_\theta^2 + 1 & 0 & 0 \\ 0 & 0 & 2c_\theta & 0 \\ 0 & 0 & 0 & 2c_\theta \end{pmatrix}, c_\theta = \cos\theta\,, \theta = \mathrm{angle}(\boldsymbol{k}_t, \boldsymbol{k}_s) \tag{6.9}$$

$$\tilde{\beta}_{FF}(\theta) = \frac{1}{4\pi(1-\delta)^2\delta^\nu}\left[\nu(1-\delta) - (1-\delta^\nu) + [\delta(1-\delta^\nu) - \nu(1-\delta)]\sin^{-2}\left({}^{\theta}/_{2}\right)\right] + \frac{1-\delta_{\theta=\pi}^\nu}{16\pi(\delta_{\theta=\pi}-1)\delta_{\theta=\pi}^\nu}(3\cos^2\theta - 1), \delta = \frac{4\sin^2(\theta/2)}{3\left(\eta_p - 1\right)^2}, \nu = \frac{3-\mu_p}{2} \qquad (6.10)$$

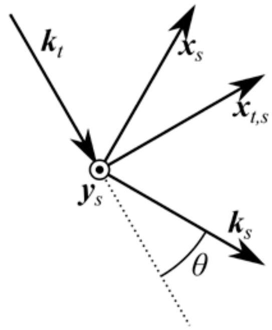

Figure 6.13 Scattering geometry.

The parameters of the Fournier-Fourand function, η_p and μ_p, are respectively the real index of refraction of the scattering particles and the slope parameter of the hyperbolic particle size distribution. The values in this work were set arbitrarily to $\eta_p = 1.08$ and $\mu_p = 3.483$ which are given as reasonable values in Ocean Optics [74]. As long as these values are kept within their typical ranges they do not significantly change the polarization angle patterns. Note that multiplying by $\tilde{\beta}(\theta)$ changes the units of $\boldsymbol{S}_s$ to (W·m^{-2}·sr^{-1}), however to return to units of (W·m^{-2}) is more complicated that simply multiplying $\boldsymbol{S}_s$ by the area per solid angle of a spherical section. This is because the volume scattering phase function is the ratio of the scattered radiant intensity per volume (W·sr^{-1}·m^{-3}) to the incident intensity (W·m^{-2}) normalized by the scattering coefficient per volume (W·m^{-3})/(W·m^{-2}). Thus, to return $\boldsymbol{S}_s$ to units of intensity, we would need to multiply it by the scattering coefficient and scattering volume to yield a radiant intensity (W·sr^{-1}), which could then be multiplied by the area per solid angle to yield an intensity. These operations do not affect the polarization angle, only the light intensity, so we neglect them here. However, they would be necessary for including propagation distance or multiple scattering.

Finally, the Stokes vector of the scattered light is transformed to the coordinate frame of the detectors, with $\boldsymbol{x}$ to the right and polarization angles increasing in the counterclockwise direction, as viewed by the detector. The detected Stokes vector is

$$\boldsymbol{S}_d = \mathbf{M}_{S\to D}\mathbf{M}_S\mathbf{M}_{R\to S}\mathbf{M}_R\boldsymbol{S}_i. \tag{6.11}$$

We assume that direct, unpolarized sunlight is the only light source, so $\boldsymbol{S}_i = (1\ 0\ \ 0\ 0)^T$, and $\boldsymbol{k}_i$ is computed using Reda and Andreas's algorithm for the apparent sun position in the sky [75]. When operating with magnetic headings, we use NOAA's Enhanced Magnetic Model to provide local fields [76].

6.3 Sun Position Inference

Our system infers the sun's position in a two-phase process. During the first phase, an initial estimate of the sun's angular position in the sky, $\hat{\rho}_s^{(1)} \in \mathbb{S}^2$, is obtained by

$$\hat{\rho}_s^{(1)} = \operatorname{argmin} \left\| \boldsymbol{\psi} \ominus \psi_m\left(\boldsymbol{\rho}_d, \hat{\rho}_s^{(1)}\right) \right\|_1 \tag{6.12}$$

where $\boldsymbol{\psi} \in \mathbb{S}^n$ is the vector of measured polarization angles at each detector orientation, $\boldsymbol{\rho}_d \in \mathbb{S}^{2\times n}$, and $\psi_m\colon (\mathbb{S}^{2\times n}, \mathbb{S}^2) \to \mathbb{S}^n$is the single-scattering model presented in §6.2. The L^1 norm is used to de-emphasize outliers caused by measurement noise. The $\ominus$ operator indicates an element-wise angular difference,

$$a \ominus b = \left(a + b + {}^{\tau}\!/_{2}\right) \operatorname{mod} \tau - {}^{\tau}\!/_{2}, \qquad a \operatorname{mod} b = a - b\left\lfloor {}^{a}\!/_{b} \right\rfloor, \tag{6.13}$$

where τ is the period of the angle (180° for polarization angles). Because the predictive power of the single-scattering model is limited, we use a kNN regression over previously measured data to learn the residuals of the single-scattering model, $\Delta\psi_m$, at the true sun position but as a function of the estimated sun position:

$$\Delta\psi_m\left(\boldsymbol{\rho}_d, \hat{\rho}_s^{(1)}\right) \approx \boldsymbol{\psi} \ominus \psi_m(\boldsymbol{\rho}_d, \rho_s). \tag{6.14}$$

The second phase of the inference algorithm uses the estimated residuals to remove model errors from the minimization to improve the inference results:

$$\hat{\rho}_s^{(2)} = \operatorname{argmin} \left\| \boldsymbol{\psi} \ominus \Delta\psi_m\left(\boldsymbol{\rho}_d, \hat{\rho}_s^{(1)}\right) \ominus \psi_m\left(\boldsymbol{\rho}_d, \hat{\rho}_s^{(1)}\right) \right\|_1 \tag{6.15}$$

$$\hat{\rho}_s^{(2)} \approx \operatorname{argmin} \left\| \psi_m(\boldsymbol{\rho}_d, \rho_s) \ominus \psi_m\left(\boldsymbol{\rho}_d, \hat{\rho}_s^{(1)}\right) \right\|_1 \tag{6.16}$$

The global position of the measurement, $\hat{\rho}_g \in \mathbb{S}^2$, can be determined from the estimated sun position by using the sun position model and searching for the latitude and longitude where the estimated sun position occurs at the time of the measurement.

$$\hat{\rho}_g = \operatorname{argmin} \operatorname{arcdist}\left(\hat{\rho}_s, \rho_s\left(\hat{\rho}_g, t\right)\right), \tag{6.17}$$

where t is the time of the measurement and $\rho_s : (\mathbb{S}^2, \mathbb{R}) \to \mathbb{S}^2$ is a model of the apparent sun position using magnetic headings, as described previously.

The inference algorithm was tested using the leave-one-out methodology. First, for each experiment, we compute $\hat{\rho}_s^{(1)}$, the naïve sun position estimate, and $\Delta\boldsymbol{\psi}_m = \boldsymbol{\psi} - \psi_m(\boldsymbol{\rho}_d, \rho_s)$, the single-scattering model residuals evaluated at the true sun position. We then separate the data into groups based on collection site and date, and for each group generate a residual estimate function, $\Delta\hat{\psi}_m(\rho_d, \rho_s)$, by training a *k*NN regression with the $\hat{\rho}_s^{(1)}$ and $\Delta\boldsymbol{\psi}_m$ from all of the data in the other groups. This residual estimate function is then used to compute the second-phase sun position estimate, $\hat{\rho}_s^{(2)}$. We chose this methodology because it allows us to test the effects of the *k*NN regression in a data-efficient manner. The data was also segregated by which sensor was used to collect it as the residuals were sufficiently dissimilar to adversely affect the results. Statistics on the global position distance errors were performed assuming a normal distribution. Statistics on the sun heading errors and sun elevation errors were performed independently, assuming a wrapped normal distribution. The first moment of the population was used to estimate the mean and variance of the normal distribution underlying the wrapped normal:

$$\bar{\boldsymbol{\theta}} = \arg m_1(\boldsymbol{\theta}), \qquad \mathrm{var}(\boldsymbol{\theta}) = -2\log|m_1(\boldsymbol{\theta})|, \qquad m_1(\boldsymbol{\theta}) = \frac{1}{n}\sum_i e^{j\theta_i} \tag{6.18}$$

The RMS statistics were then computed using the mean and variance as

$$\mathrm{RMS}(\boldsymbol{\theta}) = \sqrt{\bar{\boldsymbol{\theta}}^2 + \mathrm{var}(\boldsymbol{\theta})}\,. \tag{6.19}$$

Significance values were determined with a paired t-test.

Statistics on the global position estimates were performed by estimating the parameters of a Kent distribution using the maximum likelihood estimation method [77]. Details are available in the online code listing.

6.4 Sensitivity Analysis

The goal of the sensitivity analysis was to determine how sensitive the instrument is to changes in polarization angle driven by movement of the apparent position of the sun in the sky. The apparent position of the sun in the sky changes over time, and changes with global position, so this analysis lets us estimate the potential positioning resolution of the system assuming a perfect inference model and based solely on the instrument’s measurement noise.

The sensitivity analysis data was collected at Dique la Quebrada, Argentina by a diver snorkeling. The instrument, configured with the fisheye lens, was mounted vertically on a tripod, similar to how it is shown in Figure 6.14. A metal disk was mounted on a small arm above the lens to block the sun and prevent the image from blooming. Data were recorded for approximately 2 hours during 2 sessions, one in the midmorning and the other in the midafternoon. The depth of the instrument, 2.5 m, was estimated by the diver. The longest continuous clean data segment from each session was used for analysis. In this case, the clean data were free from animals or foreign objects, and were recorded while the sun was not obscured by clouds.

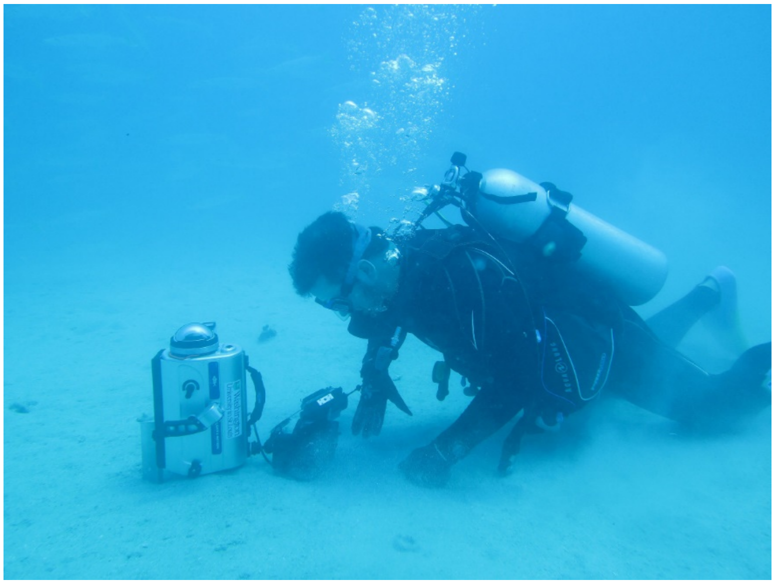

Figure 6.14 The camera configured with a dome port and fisheye lens. The metal disk to block the sun is not included in the picture.

These videos were processed by taking the average polarization state from circular regions placed every 6° of heading around the periphery of the image at approximately 7.5° above the horizontal plane, as shown in Figure 6.15. Data from regions where the partial polarization dipped below 5% were discarded. The short duration of the time-series allows us to model the polarization angles using a Gaussian process with a linearly-changing mean and stationary covariance:

$$\boldsymbol{\psi}(t) \in \mathbb{S}^n \sim \mathcal{N}(\boldsymbol{\psi}_0 + \boldsymbol{\psi}_1 t, \boldsymbol{\Sigma}). \qquad (6.20)$$

Figure 6.15 An intensity image taken during the sensitivity experiment. The black disk in the center is to block the sun from over-exposing the image. The colored dots around the periphery show the sampling locations for the analysis. Sampling locations were rejected if the DoLP drops below 5% at any point during the analysis.

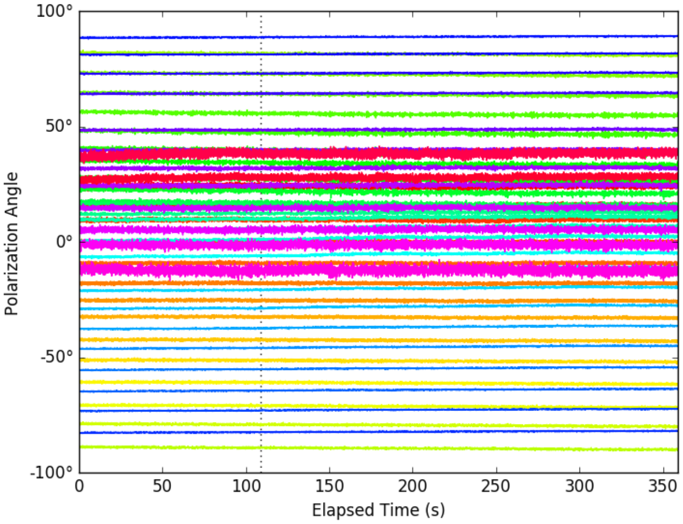

Figure 6.16 Polarization angle traces taken during one of the sensitivity experiments. The color of each trace corresponds to its sample location, as in Figure 6.15. The dotted vertical line indicates the elapsed time for the instrument to detect the change in polarization angles with 99% confidence.

The parameters of the mean are estimated with a linear least-squares regression on the measured angles, unwrapped so that there are no discontinuities between 180° and 0°. The covariance matrix is estimated from the regression's residuals. For determining instrument sensitivity, we use the Mahalanobis distance metric to perform hypothesis testing on the measurements:

$$D_M(\boldsymbol{\psi}(t), \overline{\boldsymbol{\psi}}) = \sqrt{(\boldsymbol{\psi}(t) - \overline{\boldsymbol{\psi}})^T \boldsymbol{\Sigma}^{-1} (\boldsymbol{\psi}(t) - \overline{\boldsymbol{\psi}})} \sim \sqrt{\chi_n^2}. \tag{6.21}$$

Given a false-rejection rate α, the χ_n^2 distribution's inverse survival function gives us the minimum Mahalanobis distance beyond which we would reject the null hypothesis H_0, that the sample was drawn from the distribution:

$$D_M(\boldsymbol{\psi}(t), \overline{\boldsymbol{\psi}}) > \sqrt{\mathrm{ISF}_{\chi_n^2}(\alpha)} \rightarrow \text{reject } H_0. \tag{6.22}$$

This metric is good for determining the instrument sensitivity because it takes into account the sensor noise and scales appropriately with the dimensionality of the measurements.

For a conservative estimate of how long it takes for the polarization angles to change sufficiently such that the instrument can detect the change with high confidence, we use the Mahalanobis distance to compare the mean polarization angles at two different times. Because the mean is a linear function, D_M can be simplified to:

$$D_M\left(\overline{\boldsymbol{\psi}}(t_b), \overline{\boldsymbol{\psi}}(t_a)\right) = |t_b - t_a| \sqrt{\boldsymbol{\psi}_1^T \boldsymbol{\Sigma}^{-1} \boldsymbol{\psi}_1}. \tag{6.23}$$

This can be combined with Eq. 6.22 to solve for the amount of time required for the mean polarization angle to change with 99% confidence:

$$\Delta t_{99\%} = \frac{\sqrt{\mathrm{ISF}_{\chi_n^2}(1\%)}}{\sqrt{\boldsymbol{\psi}_1^T \boldsymbol{\Sigma}^{-1} \boldsymbol{\psi}_1}}. \tag{6.24}$$

Because this change in polarization angles is driven by the movement of the sun, we claim that under similar conditions, the instrument can detect changes in sun position of the same magnitude as that which occurred over the $\Delta t_{99\%}$ interval during the experiment. We can further estimate the instrument's sensitivity to changes in location by computing the linear distance the earth rotates relative to the sun over $\Delta t_{99\%}$ at the latitude of the experiment. The results of both sensitivity experiments are summarized in

	$\Delta t_{99\%}$	Sun Movement	Ground Distance
Experiment 1	88.5 s	0.31°	35.2 km
Experiment 2	108.6 s	0.38°	43.1 km

Table 6.4 Sensitivity Results.

Chapter 7: Conclusions

Over the course of my doctorate studies I have designed and built a functional and robust underwater polarization video camera system that has been used successfully for over 46 hours of data recordings in the field. The system is based on a bio-inspired polarization sensor that I helped develop, and includes real-time polarization image processing software for displaying live polarization video to the operator. I have also developed a suite of post-processing software for analyzing the data recorded by the system.

Using this system, I have shown that it is possible to use the polarization patterns of the underwater light outside of Snel's window to infer the apparent position of the sun in the sky. Using my method, the estimated sun's position can be used as a compass or for determining global position with moderate accuracy, around 440 km RMS. My investigations into the instrument's sensitivity show that it is capable of detecting changes in polarization state corresponding to approximately 45 km of ground movement. This means that a majority of the position error can be attributed to the modelling inaccuracies and the inference algorithm.

The single-scattering model is a clear target for improvement, as it neglects known physical phenomena such as the contributions of skylight and multiple scattering effects. Regarding the inference algorithm, additional training data could be used to improve the estimates of the model residuals, but it is likely that more significant improvements would be gained by inferring sun trajectories over time rather than single sun positions.

This research settles a long-standing research problem—whether or not it is possible to navigate using the in-water polarization patterns—that was first posed in 1956 [23]. By showing that it is possible to infer the sun's position I have provided a proof-of-concept for a new mode of underwater navigation that could be used in conjunction with other technologies to improve their performance. In addition, this work gives insight into the ways that marine animals with polarization-sensitive vision could perform both local and long-distance navigation.

References

[1] E. G. R. Taylor, *The Haven-Finding Art: A History of Navigation from Odysseus to Captain Cook*. New York: Abelard-Shuman Limited, 1957,

[2] M. S. Grewal, L. R. Weill, and A. P. Andrews, *Global Positioning Systems, Inertial Navigation, and Integration*. Wiley, 2007. doi: 10.1002/0471200719

[3] R. C. Smith and K. S. Baker, "Optical properties of the clearest natural waters (200-800 nm)," *Applied optics*, vol. 20, no. 2, p. 177, 1981. doi: 10.1364/AO.20.000177

[4] B. Kelley and K. Naishadham, "RF multicarrier signaling and antenna systems for low SNR broadband underwater communications," ed, 2013, pp. 240-242. doi: 10.1109/SiRF.2013.6489492

[5] I. S. Bogie, "Conduction and Magnetic Signalling in the Sea. A Background Review," *Radio and Electronic Engineer*, vol. 42, no. 10, pp. 447-452, 1972. doi: 10.1049/ree.1972.0076

[6] A. I. Al-Shamma'a, A. Shaw, and S. Saman, "Propagation of electromagnetic waves at MHz frequencies through seawater," *IEEE Transactions on Antennas and Propagation*, vol. 52, no. 11, pp. 2843-2849, 2004. doi: 10.1109/TAP.2004.834449

[7] F. H. Fisher, "Sound absorption in sea water a)," *Journal of the Acoustical Society of America*, vol. 62, no. 3, pp. 558-564, 1977. doi: 10.1121/1.381574

[8] L. Whitcomb, D. Yoerger, H. Singh, and J. Howland, "Advances in underwater robot vehicles for deep ocean exploration: Navigation, control, and survey operations," in *Navigation, Control and Survery Operations," in The Ninth International Symposium on Robotics Research*, 1999: Citeseer. doi: 10.1007/978-1-4471-0765-1_53

[9] L. Whitcomb, D. Yoerger, and H. Singh, "Advances in Doppler-based navigation of underwater robotic vehicles," in *Robotics and Automation, 1999. Proceedings. 1999 IEEE International Conference on*, 1999, vol. 1, pp. 399-406: IEEE. doi: 10.1109/ROBOT.1999.770011

[10] (2013). *Interface Specification IS-GPS-200: Navstar GPS Space Segment/Navigation User Interfaces*.

[11] W. Chow, J. Gea-Banacloche, L. Pedrotti, V. Sanders, W. Schleich, and M. Scully, "The ring laser gyro," *Reviews of Modern Physics,* vol. 57, no. 1, p. 61, 1985. doi: 10.1103/RevModPhys.57.61

[12] A. S. Gerges, T. P. Newson, J. D. C. Jones, and D. A. Jackson, "High-sensitivity fiber-optic accelerometer," *Optics Letters,* vol. 14, no. 4, pp. 251-253, 1989/02/15 1989. doi: 10.1364/OL.14.000251

[13] D. Goshen-Meskin and I. Y. Bar-Itzhack, "Unified approach to inertial navigation system error modeling," *Journal of Guidance, Control, and Dynamics,* vol. 15, no. 3, pp. 648-653, 1992. doi: 10.2514/6.1990-3367

[14] L. Paull, S. Saeedi, M. Seto, and H. Li, "AUV Navigation and Localization: A Review," *IEEE Journal of Oceanic Engineering,* vol. 39, no. 1, pp. 131-149, 2014. doi: 10.1109/JOE.2013.2278891

[15] B. Lascelles *et al.*, "Migratory marine species: their status, threats and conservation management needs," *Aquatic Conservation: Marine and Freshwater Ecosystems,* vol. 24, no. S2, pp. 111-127, 2014. doi: 10.1002/aqc.2512

[16] T. Labhart and E. P. Meyer, "Neural mechanisms in insect navigation: polarization compass and odometer," *Current Opinion in Neurobiology*, vol. 12, no. 6, pp. 707-714, 2002. doi: 10.1016/s0959-4388(02)00384-7

[17] S. Rossel and R. Wehner, "The bee's map of the e-vector pattern in the sky," *Proceedings of the National Academy of Sciences*, vol. 79, no. 14, pp. 4451-4455, 1982. doi: 10.1073/pnas.79.14.4451

[18] B. el Jundi, J. Smolka, E. Baird, M. J. Byrne, and M. Dacke, "Diurnal dung beetles use the intensity gradient and the polarization pattern of the sky for orientation," *The Journal of Experimental Biology*, vol. 217, no. 13, pp. 2422-2429, 2014. doi: 10.1242/jeb.101154

[19] M. Dacke, T. A. Doan, and D. C. O'Carroll, "Polarized light detection in spiders," *Journal of Experimental Biology*, vol. 204, no. 14, pp. 2481-2490, 2001. jeb.biologists.org/content/204/14/2481

[20] F. R. Moore and J. B. Phillips, "Sunset, skylight polarization and the migratory orientation of yellow-rumped warblers, Dendroica coronata," *Animal Behaviour*, vol. 36, no. 6, pp. 1770-1778, 11// 1988. doi: 10.1016/S0003-3472(88)80116-7

[21] R. Muheim, "Behavioural and physiological mechanisms of polarized light sensitivity in birds," *Philosophical Transactions of the Royal Society of London B: Biological Sciences*, vol. 366, no. 1565, pp. 763-771, 2011. doi: 10.1098/rstb.2010.0196

[22] V. A. Timofeeva, "Optics of turbid waters (results of laboratory studies)," *Optical Aspects of Oceanography*, 1974. lccn.loc.gov/73007038

[23] T. H. Waterman and W. E. Westell, "Quantitative Effect of the Sun's Position on Submarine Light Polarization," *Journal of Marine Research*, vol. 15, no. 2, pp. 149-169, 1956.

[24] C. W. Hawryshyn, "Polarization Vision in Fish," *American Scientist*, vol. 80, no. 2, pp. 164-175, 1992. www.jstor.org/stable/29774602

[25] G. Horváth and D. Varjú, *Polarized light in animal vision: polarization patterns in nature*. Springer, 2004. doi: 10.1007/978-3-662-09387-0

[26] N. Shashar, R. Hagan, J. G. Boal, and R. T. Hanlon, "Cuttlefish use polarization sensitivity in predation on silvery fish," *Vision Research*, vol. 40, no. 1, pp. 71-75, 1// 2000. doi: 10.1016/S0042-6989(99)00158-3

[27] G. M. Calabrese, P. C. Brady, V. Gruev, and M. E. Cummings, "Polarization signaling in swordtails alters female mate preference," *Proceedings of the National Academy of Sciences*, vol. 111, no. 37, pp. 13397-13402, September 16, 2014 2014. doi: 10.1073/pnas.1321368111

[28] T. W. Cronin, N. Shashar, R. L. Caldwell, J. Marshall, A. G. Cheroske, and T.-H. Chiou, "Polarization Vision and Its Role in Biological Signaling," *Integrative and Comparative Biology*, vol. 43, no. 4, pp. 549-558, August 1, 2003 2003. doi: 10.1093/icb/43.4.549

[29] D. C. Parkyn, J. D. Austin, and C. W. Hawryshyn, "Acquisition of polarized-light orientation in salmonids under laboratory conditions," *Animal behaviour*, vol. 65, no. 5, pp. 893-904, 2003. doi: 10.1006/anbe.2003.2136

[30] T. H. Waterman, "Polarization of scattered sunlight in deep water," *Deep Sea Research*, vol. 3, pp. 426-434, 1955.

[31] A. Lerner, S. Sabbah, C. Erlick, and N. Shashar, "Navigation by light polarization in clear and turbid waters," *Philosophical Transactions of the Royal Society of London B: Biological Sciences*, vol. 366, no. 1565, pp. 671-679, 2011. doi: 10.1098/rstb.2010.0189

[32] T. York *et al.*, "Bioinspired polarization imaging sensors: From circuits and optics to signal processing algorithms and biomedical applications," *Proceedings of the IEEE,* vol. 102, no. 10, pp. 1450-1469, 2014. doi: 10.1109/JPROC.2014.2342537

[33] S. B. Powell and V. Gruev, "Calibration methods for division-of-focal-plane polarimeters," *Optics Express,* vol. 21, no. 18, pp. 21039-21055, 2013. doi: 10.1364/OE.21.021039

[34] T. York, S. B. Powell, and V. Gruev, "A comparison of polarization processing across different platforms," vol. 8160, ed, 2011. doi: 10.1117/12.894633

[35] N. W. Roberts *et al.*, "Animal Polarization Imaging and Implications for Optical Processing," *Proceedings of the IEEE,* 2014. doi: 10.1109/JPROC.2014.2341692

[36] S. Johnsen, Y. L. Gagnon, N. J. Marshall, T. W. Cronin, V. Gruev, and S. Powell, "Polarization vision seldom increases the sighting distance of silvery fish," *Current Biology,* vol. 26, no. 16, pp. R752-R754, 8/22/ 2016. doi: 10.1016/j.cub.2016.07.030

[37] S. E. Temple *et al.*, "Perceiving polarization with the naked eye: characterization of human polarization sensitivity," in *Proc. R. Soc. B*, 2015, vol. 282, no. 1811, p. 20150338: The Royal Society. doi: 10.1098/rspb.2015.0338

[38] G. G. Stokes, "On the change of refrangibility of light," *Philosophical Transactions of the Royal Society of London*, vol. 142, pp. 463-562, 1852. doi: 10.1098/rstl.1852.0022

[39] K. Oka and N. Saito, "Snapshot complete imaging polarimeter using Savart plates," 2006, vol. 6295, pp. 629508-629508-7. doi: 10.1117/12.683284

[40] F. Snik, T. Karalidi, and C. U. Keller, "Spectral modulation for full linear polarimetry," *Applied Optics,* vol. 48, no. 7, pp. 1337-1346, 2009. doi: 10.1364/ao.48.001337

[41] J. S. Tyo, "Design of optimal polarimeters: maximization of signal-to-noise ratio and minimization of systematic error," *Applied Optics,* vol. 41, no. 4, pp. 619-630, 2002/02/01 2002. doi: 10.1364/AO.41.000619

[42] J. S. Tyo, D. L. Goldstein, D. B. Chenault, and J. A. Shaw, "Review of passive imaging polarimetry for remote sensing applications," *Applied Optics,* vol. 45, no. 22, pp. 5453-5469, 08/01 2006. doi: 10.1364/AO.45.005453

[43] A. G. Andreou and Z. K. Kalayjian, "Polarization imaging: principles and integrated polarimeters," *IEEE Sensors journal,* vol. 2, no. 6, pp. 566-576, 2002. doi: 10.1109/JSEN.2003.807946

[44] J. S. Tyo, C. F. LaCasse, and B. M. Ratliff, "Total elimination of sampling errors in polarization imagery obtained with integrated microgrid polarimeters," *Opt. Lett.,* vol. 34, no. 20, pp. 3187-3189, 10/15 2009. doi: 10.1364/OL.34.003187

[45] B. M. Ratliff, C. F. LaCasse, and J. S. Tyo, "Interpolation strategies for reducing IFOV artifacts in microgrid polarimeter imagery," *Optics express,* vol. 17, no. 11, pp. 9112-9125, 2009. doi: 10.1364/OE.17.009112

[46] S. Gao and V. Gruev, "Gradient-based interpolation method for division-of-focal-plane polarimeters," *Opt. Express,* vol. 21, no. 1, pp. 1137-1151, 01/14 2013. doi: 10.1364/OE.21.001137

[47] E. Gilboa, J. P. Cunningham, A. Nehorai, and V. Gruev, "GP-grid image interpolation and denoising for division of focal plane sensors," in *SPIE Sensing Technology+ Applications,* 2014, pp. 909905-909905-6: International Society for Optics and Photonics. doi: 10.1117/12.2050615

[48] S. Gao, R. Njuguna, and V. Gruev, "Fabrication and performance evaluation of pixelated nano-wire grid polarizer," 2013, vol. 8873, pp. 88730L-88730L-7. doi: 10.1117/12.2023115

[49] T. York and V. Gruev, "Characterization of a visible spectrum division-of-focal-plane polarimeter," *Applied Optics,* vol. 51, no. 22, pp. 5392-5400, 08/01 2012. doi: 10.1364/AO.51.005392

[50] X. Xu, M. Kulkarni, A. Nehorai, and V. Gruev, "A correlation-based interpolation algorithm for division-of-focal-plane polarization sensors," *Proc. SPIE,* vol. 8364, pp. 83640L-83640L, 2012. doi: 10.1117/12.919196

[51] Y. L. Gagnon and N. J. Marshall, "Intuitive representation of photopolarimetric data using the polarization ellipse," *Journal of Experimental Biology,* vol. 219, no. 16, pp. 2430-2434, 2016. doi: 10.1242/jeb.139139

[52] O. A. R. Board, "OpenMP Application Program Interface," 3.0 ed, 2008, www.openmp.org/mp-documents/spec30.pdf

[53] J. Nickolls, I. Buck, M. Garland, and K. Skadron, "Scalable Parallel Programming with CUDA," *Queue,* vol. 6, no. 2, pp. 40-53, 2008. doi: 10.1145/1365490.1365500

[54] Xilinx, "LogiCORE CORDIC," 4.0 ed, 2011,

[55] A. El Gamal, B. A. Fowler, H. Min, and X. Liu, "Modeling and estimation of FPN components in CMOS image sensors," *Proc. SPIE,* vol. 3301, pp. 168-177, 1998. doi: 10.1117/12.304560

[56] V. Gruev, Z. Yang, J. Van der Spiegel, and R. Etienne-Cummings, "Current mode image sensor with two transistors per pixel," *Circuits and Systems I: Regular Papers, IEEE Transactions on,* vol. 57, no. 6, pp. 1154-1165, 2010. doi: 10.1109/TCSI.2009.2030093

[57] V. Gruev, "Fabrication of a dual-layer aluminum nanowires polarization filter array," *Opt. Express,* vol. 19, no. 24, pp. 24361-24369, 11/21 2011. doi: 10.1364/OE.19.024361

[58] J. J. Wang, F. Walters, X. Liu, P. Sciortino, and X. Deng, "High-performance, large area, deep ultraviolet to infrared polarizers based on 40 nm line/78 nm space nanowire grids," *Applied Physics Letters,* vol. 90, no. 6, pp. 061104-061104-3, 2007. doi: 10.1063/1.2437731

[59] M. A. Jensen and G. P. Nordin, "Finite-aperture wire grid polarizers," *J. Opt. Soc. Am. A,* vol. 17, no. 12, pp. 2191-2198, 12/01 2000. doi: 10.1364/JOSAA.17.002191

[60] V. Gruev, R. Perkins, and T. York, "CCD polarization imaging sensor with aluminum nanowire optical filters," *Optics Express,* vol. 18, no. 18, pp. 19087-19094, 08/30 2010. doi: 10.1364/OE.18.019087

[61] "KAI-2020 Image Sensor Device Performance Specification," Revision 4.0 MTD/PS-0692 ed: Eastman Kodak Company, 2010,

[62] T. H. Group. (1997-2017). *Hierarchical Data Format, version 5*. Available: www.hdfgroup.org/HDF5

[63] N. G. Jerlov, "Oceanic Light Scattering Properties Related To Dynamic Conditions," *Optical Engineering,* vol. 8, no. 3, pp. 080389-080389-, 1970. doi: 10.1117/12.7971519

[64] T. Labhart and E. P. Meyer, "Detectors for polarized skylight in insects: a survey of ommatidial specializations in the dorsal rim area of the compound eye," *Microscopy research and technique,* vol. 47, no. 6, pp. 368-379, 1999. doi: 10.1002/(sici)1097-0029(19991215)47:6<368::aid-jemt2>3.3.co;2-h

[65] A. Ivanoff and T. H. Waterman, "Factors, Mainly Depth and Wavelength, Affecting the Degree of Underwater Light Polarization," *Journal of Marine Research*, vol. 16, no. 3, pp. 283-307, 1958.

[66] P. C. Brady *et al.*, "Open-ocean fish reveal an omnidirectional solution to camouflage in polarized environments," *Science*, vol. 350, no. 6263, pp. 965-969, 2015. doi: 10.1126/science.aad5284

[67] T. H. Waterman, "Reviving a neglected celestial underwater polarization compass for aquatic animals," *Biological Reviews*, vol. 81, no. 01, pp. 111-115, 2006. doi: 10.1017/S1464793105006883

[68] E. Boss, C. Roesler, and L. Taylor. (2010). *Optical Constituents of the Ocean*. Available: www.oceanopticsbook.info/view/optical_constituents_of_the_ocean

[69] M. Born and E. Wolf, *Principles of Optics*, 7th expanded ed. 1999,

[70] N. S. Altman, "An introduction to kernel and nearest-neighbor nonparametric regression," *The American Statistician*, vol. 46, no. 3, pp. 175-185, 1992. doi: 10.2307/2685209

[71] N. G. Jerlov, *Optical Oceanography* (Elsevier Oceanography Series, no. 5). 1968. doi: 10.1016/s0422-9894(08)70923-1

[72] D. Lambrinos, R. Möller, T. Labhart, R. Pfeifer, and R. Wehner, "A mobile robot employing insect strategies for navigation," *Robotics and Autonomous systems*, vol. 30, no. 1, pp. 39-64, 2000. doi: 10.1016/S0921-8890(99)00064-0

[73] M. Collett and T. S. Collett, "How do insects use path integration for their navigation?," *Biological cybernetics*, vol. 83, no. 3, pp. 245-259, 2000. doi: 10.1007/s004220000168

[74] C. D. Mobley *et al.*, "Comparison of numerical models for computing underwater light fields," *Applied Optics*, vol. 32, no. 36, pp. 7484-7504, 1993/12/20 1993. doi: 10.1364/AO.32.007484

[75] I. Reda and A. Andreas, "Solar position algorithm for solar radiation applications," *Solar Energy,* vol. 76, no. 5, pp. 577-589, // 2004. doi: 10.1016/j.solener.2003.12.003

[76] A. Chulliat, P. Alken, M. Nair, A. Woods, and S. Maus, "The Enhanced Magnetic Model 2015-2020," *National Centers for Environmental Information, NOAA,* 2015. doi: 10.7289/V56971HV

[77] P. Kasarapu, "Modelling of directional data using Kent distributions," *arXiv preprint arXiv:1506.08105,* 2015.